

Magnetically Controlled Scalable Micro-Robots  
FYDP Final Report

Nanotechnology Engineering  
Fourth Year Design Project Proposal  
NE 409  
Presented to Dr. Hany Aziz  
03/04/2023

Group 16

Patrick Hafenberg

20785592

pahafenb



Karim Habashy

20783464

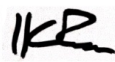
khabashy



Ian Ross

20771636

ikross



Agosh Saini

20785161

as7saini



Consultant:  
Professor Hamed Shahsavan

*This report is submitted as the final report requirement for the NE 409 course. It has been written solely by us and has not been submitted for academic credit before (other than appendices A-F) at this or any other academic institution.*

## Executive Summary

The aim of this FYDP is the achievement of scalable microrobot actuation using generated magnetic multipoles. The project is divided into two main components, the creation of a controller actuating microbots and fabrication of the controlled actuators. The controller will supply a magnetic field to a central arena using 6 surrounding electromagnets through which a DC current is applied. The second is microrobot fabrication, which consists of the design of a microbots with adjustable morphology controlled by applied field, with controllable configuration and motion.

This project is motivated by potential applications within the medical domain, including minimally invasive surgery. By creating microrobots granted multiple degrees of freedom to operate, invasive surgery can be avoided, leading to much shorter recovery times and potential for post operation infection.

Since the project is focused on the medical industry, design criteria include high resolution of magnetic field enabling sophisticated actuator control, system stability, and considerations of biocompatibility. The deliverable of this project is a prototype capable of generating and controlling the required magnetic field, and a central arena populated with responsive actuators.

## Acknowledgements

We would like to acknowledge the assistance received in carrying out this design project thus far from Dr. Hamed Shahsavani who has been our supervisor who has generously provided us with the knowledge and resources needed to support our work. We thank Dr. Mahla Poudineh for SU8 and associated reagents. Furthermore, we would also like to thank Dr. Bahareh Sadeghimakki for providing AZ3330. We are also grateful for Dr. Hany Aziz who has provided help in the structuring of our FYDP submissions, as well as providing feedback in areas that we can improve in. Lastly, we would like to thank Derek Muller from the YouTube channel Veritasium for inspiration for this project.

## Glossary of Terms and Acronyms

DOF	Degree of freedom.
Arena	Arena: The inner space of our system in which the magnetic field is controlled. The arena is also the work envelope to which our actuators are restricted.
MagneToad	Portmanteau of “magnetic electrode”. Used to describe the Iron probes that conduct magnetic flux into the arena.
Multipole	A linear basis system used to represent harmonic functions with angular periodicity. Our system uses multipoles that cycle one to three times around the arena’s perimeter.
Normal Multipole	A multipole term that has maximum amplitude at the first probe.
Skew Multipole	A multipole term that has zero amplitude at the first probe.
microbots	Portmanteau for “micro robot”. Describes individual actuators within our system.

## Table of Contents

<b><i>Executive Summary</i></b> .....	<b>2</b>
<b><i>Acknowledgements</i></b> .....	<b>3</b>
<b><i>Glossary of Terms and Acronyms</i></b> .....	<b>4</b>
<b><i>List of Figures</i></b> .....	<b>7</b>
<b><i>List of Tables</i></b> .....	<b>8</b>
<b><i>List of Equations</i></b> .....	<b>9</b>
<b><i>Introduction</i></b> .....	<b>10</b>
Customer requirements .....	13
<b><i>Discussion</i></b> .....	<b>14</b>
<b>Design Description</b> .....	<b>15</b>
High Level .....	15
Low Level .....	19
<b>Design Verification</b> .....	<b>23</b>
High Level .....	23
Low Level .....	24
<b>Prototype Construction</b> .....	<b>26</b>
<b>Test Results</b> .....	<b>29</b>
<b>Deviations / Shortfalls</b> .....	<b>30</b>
<b>Actuators</b> .....	<b>33</b>
Design Description.....	33
Design Verification.....	34
Actuator Prototype Construction .....	38
Test Results.....	41
Deviations and Shortfalls.....	42
<b><i>Summary</i></b> .....	<b>42</b>
<b><i>References</i></b> .....	<b>46</b>
<b><i>Appendices</i></b> .....	<b>1</b>
<b>Appendix A</b> .....	<b>1</b>
<i>Customer Requirements</i> .....	1
References .....	6
<b>Appendix B</b> .....	<b>1</b>
Verification Plan .....	1
<b>Appendix C</b> .....	<b>1</b>
Test Plan for the Constructed Design Prototype.....	1
<b>Appendix D</b> .....	<b>1</b>
Preliminary Design Specifications .....	1
References .....	14

<b>Appendix E</b> .....	<b>1</b>
Verification Data.....	1
<b>Appendix F</b> .....	<b>1</b>
Prototype Test/Measurement Data .....	1
<b>Appendix G</b> .....	<b>1</b>
FYDP Resources .....	1

## List of Figures

FIGURE 1: JILES-ATHERTON HYSTERESIS CURVE. SLOPE INTERSECTS THE CURVE AT POSITIVE AND NEGATIVE POINTS OF RELUCTANCE. ....	17
FIGURE 2: DESIGNED CONTROL LOOP .....	17
FIGURE 3: ALTERNATIVE HYSTERESIS MODELS USING CIRCULAR (LEFT) AND AFFINE (RIGHT) MODELS. ....	19
FIGURE 4: MACHINED IRON PARTS HELD TOGETHER USING MACHINE CUT HDPE (LEFT). COIL WINDINGS ADDED TO THE IRON CORES (RIGHT).....	27
FIGURE 5: MICROBOT CONTROLLER HARDWARE COMPARTMENT AND FINAL PROTOTYPE.....	28
FIGURE 6: THIN FILM STRUCTURE OF ACTUATOR.....	39
FIGURE 7: BEADING OF DLP RESIN.....	39
FIGURE 8: ISSUE WITH PATTERN TRANSFERRING ONTO SU8 .....	40
FIGURE 9: OIL BEAD ACTUATORS .....	40

## List of Tables

TABLE 1: LOW-LEVEL TEST RESULTS VERSUS CUSTOMER REQUIREMENTS.....	30
TABLE 2: CUSTOMER REQUIREMENTS FOR ACTUATORS .....	42

## List of Equations

EQUATION 1- STABILITY CRITERIA.....	38
EQUATION 2 - PARAMAGNETIC THICKNESS.....	38

## Introduction

Across implementations, any robot can be viewed as a self-contained system that performs tasks with some degree of autonomy. For small-scale robotics, it becomes increasingly difficult for such a system to achieve both, as the ability for any self-contained system to perform logical operations and store energy decreases rapidly with size.

This fundamental limitation in small scale robotics is reflected in the current state of the art. Most, if not all approaches forego a system that is self-contained to one that merely appears to be. This is achieved by providing control and power through an external field, be it acoustic, electric, magnetic, or otherwise. By providing control through this external field, control logic and power supply can be physically separated from the actuators. This converts the issue of producing smaller robots to an issue of controlling a physical field, which is much simpler. Such systems can be evaluated under the following criteria:

1. (Autonomy) No part of the controller can extend into the work envelope, and the system must operate with obstructions present.
2. (Sophistication) Actuator configuration must exhibit multiple local DOF.
3. (Stability) Configurations of actuators must exhibit stable equilibrium.
4. (Scale) Must apply to actuators of vanishing volume and of various amounts.
5. (Non-invasive) Local actuation must not require changes to the local environment.

These criteria ultimately define a system that is functionally equivalent to a self-contained robot at small sizes. To date, no system has been produced which can satisfy all 5 proposed requirements, with most systems satisfying only 3 or 4.

- Systems with primarily paramagnetic actuators aren't stable (Earnshaw's theorem). [1] [2]
- Hui et al.'s swarm microrobots require visual feedback for control due to instability. [3]
- Xin et al.'s magnetically controlled soft robots require local pH changes to actuate. [4]
- MEMS actuators aren't autonomous (controller occupies work envelope).
- Traditional robots require a minimum volume for onboard logic & energy storage.

We hereby propose a system in which actuators are controlled via an arbitrarily complex magnetic field, which is controlled and measured over the work envelope's boundary. In a practical system, changes in the actuation field occur relatively slowly (RF actuation fields are damped by hydrodynamic interactions), allowing the interior of the work envelope to be modeled as magnetoquasistatic.

In the absence of currents (or ferromagnetic materials) within the work envelope, its magnetic field has both zero divergence and zero curl. Thus, it is explicitly determined by its boundary conditions, with the resolution of the boundary conditions ultimately determining the complexity of magnetic field that can be achieved. Such a magnetic field can be described as the gradient of a scalar field, akin to voltage, with the added restriction that any closed region of space has zero net potential.

Within such a field, paramagnets reach a stable equilibrium at local maxima, and likewise for diamagnets with minima. Earnshaw's theorem states that such a field cannot have local maxima, making paramagnetic actuators inherently unstable. Although diamagnetic actuators can be stably confined, their stable configuration is a set of points which limits the local DOFs that they can stably occupy. We therefore design actuators that are comprised of a larger diamagnet rigidly connected to a smaller paramagnet. The paramagnetic region of the actuator is pulled towards the work envelope's boundary, expanding the stable configuration from a point to a closed curve.

Local DOF are expressed through the number and shape of these curves.

Our actuators are highly sensitive to the relative amounts of diamagnet and paramagnet they contain. On top of this, diamagnetic materials are much weaker than paramagnetic ones. To address this, our system will see the actuators suspended in a paramagnetic solution. In a magnetic field, the solution around the actuators is pulled, effectively pushing our actuators in the opposite direction in the same fashion that a ship is pushed upwards by the water it displaces. This is known as the Magneto-Archimedes principle. Using this, we can use diamagnetic photoresist, and easily tune the diamagnet/paramagnet ratio of our actuators by diluting the solution, as well the ratios of their diamagnet/paramagnet components themselves.

Our system can, in principle, produce arbitrarily complex configurations of nano-scale actuators in 3D. To maximize our chance of success in our project, we have devised a minimum viable product which satisfies our five functional criteria. This implementation consists of an array of 6 electromagnets to control the boundary, which allows for up to 5 local DOF. The designed actuators in our implementation consist of stacked cylinders of Ni and SU-8, suspended in a paramagnetic solution of manganese (ii) and iron (ii) acetate.

To implement the system, the components above need to be enclosed to be presented as a single prototype. This means that the power source, logic (provided by microcontrollers), feedback magnetic sensors, electromagnets, and beaker containing the solution and actuators all need to be housed and mounted in a box/physical enclosure.

## Customer requirements

This system addresses the customer requirements in a way such that it may serve as an overarching framework with modular sub-systems. Through interviews with industry experts and our literature review, we came to the following system requirements. These requirements fall under biocompatibility, locomotion, and control. An expanded version can be found in Appendix A. The system was created with certain evaluation criteria as mentioned above. These criteria can be elaborated upon for the various subsystems into customer requirements.

The first requirement, autonomy, is the central principle of this project. Since we aim to achieve it using electromagnetic controllers, the controllers are required to exhibit sufficient strength to the central arena to enable control of the actuators. Sophistication of our system is achieved through intuitive control of the microbots. From a user point of view, this will be in the form of an input desired configuration. This will be given via commands using an x-box controller. Using the controller, the direction of movement can be determined via joystick, triggers can be used to focus the microbots and determine the direction they face, etc. From a device perspective, the precise motion that can only be achieved through vectorization of the robots using paramagnetic and diamagnetic components together. This is also only possible with the high degree of freedoms achieved using 6 electromagnets.

For biocompatibility, the ideal materials used would be required to be FDA approved. However, as this is still a proof of concept and due to budget constraints, we have settled for non-toxic materials. While we employ the Magneto-Archimedes principle by making the solution paramagnetic, this is done to improve prototype performance with the relatively low magnetic field generated by the solenoids.

To meet the requirement of biocompatibility, as well as efficient control, we take advantage of the inherent stability of diamagnetic materials (versus unstable paramagnets), as they are much simpler to control in case of deviations in the system from given states. This relaxes the complexity and necessity of the control system needed for error correction.

Finally, we design our system to be scalable both in size of arena, as well as size of actuators. When considering applications in minimally invasive surgery, patients would need to physically occupy the scaled-up version of the arena to allow for control of microbots in their bodies. This implies that the system needs to be scaled to a 3D cylindrical space. In theory, this is possible based on the principles we employ in design, as the only change would be in the configuration and number of electromagnets and probes used to generate and guide the magnetic field. On the other hand, the actuators also have an element of scalability to be considered: since the microbots are composed of magnetically responsive materials, their volume is purely limited by their ability to align and be steered by a magnetic field. Therefore, it should be possible to use actuators of various sizes while maintaining control over them.

## Discussion

Broadly speaking, the prototype to be built comprises 2 subsystems: The microbot actuators, and the electromagnet system controlling them. The actuators are discussed in the next section, while the electromagnet is further split into high- and low-level system and discussed below.

From an outsider perspective, users control the system we have built through inputs indicating specific desired motion of the microbots. In our system, these external commands have to be translated into currents for the coil drive. Using Ampere's Law and a hysteresis model, a scalar field is calculated to define basis vectors that in turn define the field of the arena in which actuator

motion can be realized. To grant the system accurate control, closed-loop feedback was designed to address errors inherent to the prototype to be built. Measures were taken to minimize this error, such as standardizing the electromagnet coil winding process, as well as confinement of the magnetization of the iron cores to the quasi-linear region of their hysteresis curves. A control loop and iterative improvement method were devised, and real-world data and COMSOL simulations were used to refine and verify the system.

The low-level system is the brains behind managing the complex magnetic field that allows users to manipulate the microbots with ease. The low-level design concept revolves around a user-friendly interface that translates high-level user inputs, such as desired configurations or movements, into real-time magnetic field adjustments. The main components of the low-level design include the user interface, magnetic field control module, and communication and integration.

Following the discussion of the design elements of the coil drive, prototype construction is outlined. The prototype consisted of electromagnets, a wooden housing, hardware, and the software components controlling the system. Test results showed varied success levels in different areas, with deviations and shortfalls including unused degrees of freedom and an incomplete PID control loop. Magnetochromic film was used for magnetic field inspection, confirming the functioning drive.

## Design Description

### High Level

The control of the actuators is given by external commands given by the user. However, these commands, relating to target direction and configuration, need to be ultimately translated to the

currents to be given to the coil drive. As described in the Controller tuning in the Verification Plan of Appendix C, to get a desired configuration, the scalar field in the arena is solved for by calculating the potential at the boundaries (namely the tips of the inner cores). This is done using Ampere's law, giving the output flux in amp-turns (I-H relation), as well as a model describing the relationship between flux and resulting field (B-H relation). For this latter relation, various models of varying complexity could be established. This is the first step: given any configuration, we can define 6 basis vectors/multipoles that can be linearly summed to produce the magnetic field matching the configuration.

Originally, closed loop control of the electromagnets was intended and planned for. Given a set state of a desired magnetic field in the arena, the coil drive would apply the appropriate current through the electromagnets, generating a flux through the iron cores. Naturally, a certain level of error was expected to propagate through the system due to non-ideal conditions.

Firstly, if wound by hand, the copper windings would have exhibited variability across different coils due to different number of coil turns. This would ultimately affect magnetic field output, requiring a different amount of current input to obtain the same magnetic flux at the tip of the iron probes. To reduce this error, the winding jig was set up to maintain as much consistency in the windings as possible. Secondly, due to saturation in the iron cores, some non-linear effect between magnetizing force and flux density due magnetic hysteresis were expected. We opted to produce a field that is confined within the linear region of the hysteretic curve seen in Figure 1: Jiles-Atherton Hysteresis Curve. Slope intersects the curve at positive and negative points of reluctance. below. Specifically, we limited the system to operate below the reluctance points (black dots) which indicate the transition into the saturation region (the main contributor of non-linear effects).

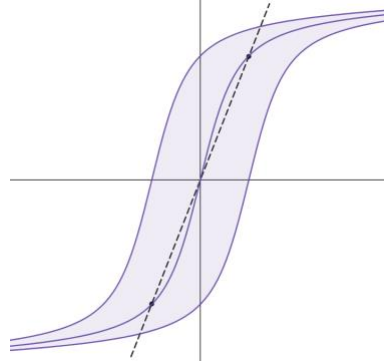


Figure 1: Jiles-Atherton Hysteresis Curve. Slope intersects the curve at positive and negative points of reluctance.

By confining the field, work done by the control loop to achieve the set state. The control loop is described as follows: Given a set magnetic field as a sum of basis vectors, current for each coil can be calculated that would output the desired field using the Teensy 4.1 controllers. This would move the system along the central hysteresis curve seen above. Using the Jiles Atherton model, this can be tracked. From here, an output field in the arena can be measured. Due to errors and non-linear effects mentioned, the output state would be expected to be inaccurate to an extent. This would then be measured using the ALS31313 Hall Effect sensors positioned at the iron probe tips. The mismatch of set and current states is then calculated, and fed as input to a standard PID controller, which outputs a new control command to the power supply. The control loop can be seen in Figure 2: Designed Control Loop.

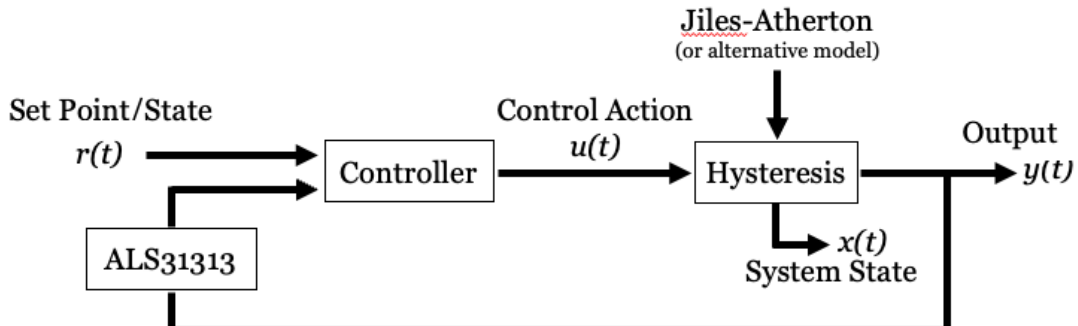


Figure 2: Designed Control Loop

The system described above would allow for error correction and give the desired accuracy needed to control the actuators as outlined in the customer requirements. It would grant the user an intuitive and simple control over the actuators in the arena because errors in the system can be accounted for, resulting in less manual feedback from the user, automating the process.

Alternatives to this are available, however. Firstly, the Jiles-Atherton model was swapped with a simpler to compute circular model. By examining the hysteresis loop in Figure 1: Jiles-Atherton Hysteresis Curve. Slope intersects the curve at positive and negative points of reluctance., we can note its resemblance to the arctan function. For values under saturation,  $2/\pi \arctan(x)$  is a very accurate representation of the linear/non-linear region. This model was useful for computations as arctan has a rational derivative, while the Langevin function does not. This simplifies the PID control significantly.

We could, in theory, have used an affine model for hysteresis of the system. To do this, a slope would be defined using the reluctance points mentioned above, with a width determined by the coercivity of the iron we use (amount of magnetization force necessary to drive the system to 0 magnetization). Hysteresis would then be represented by an affine translation of the anhysteretic slope [5]. This would have posed too much inaccuracy in the system, leading to an overreliance on the PID controller. Furthermore, it performs very poorly for any field calculations past reluctance, which is the main contribution of the hysteresis model in the first place. The circular and affine models described can be seen in Figure 3: Alternative hysteresis models using circular (left) and affine (right) models.

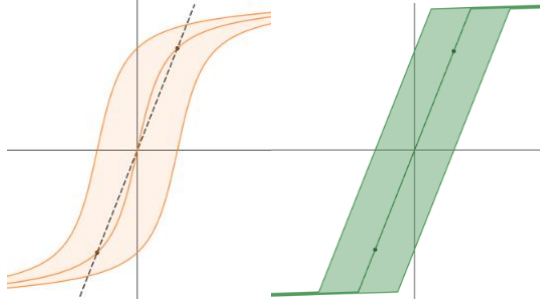


Figure 3: Alternative hysteresis models using circular (left) and affine (right) models.

The other alternative to the system is having open loop control. While this is not ideal, it serves as a contingency plan in case issues present themselves in lower levels of the system. Customer requirements may still be met, however, due to our consideration of Earnshaw's theorem. If the particles used were paramagnetic, they would be controlled by being pulled to local maxima of the magnetic field created in the arena. This would be unstable: slight deviations from the target field lead would lead the particles to stray away from the field. It would have also limited the number of particles possible to confine within the region of the maxima. Since we use diamagnetic actuators, however, they find equilibrium at local minima of the field instead, being pushed away from the field. In this scenario, inaccuracies in the produced field can still lead to configurations close to the set state. Furthermore, the considerations taken in operating within the linear region of the hysteresis curve as well as the systematicity of creating the coils using the designed winding jig reduce the error in the designed system.

## Low Level

Starting with the user interface, both a live-camera view of the microbots, and an intuitive controller are used. Starting with the visualization using the live-camera feed, a magnified camera system was used to see the microbots due to the nature of their small size. The camera system

consists of a high-resolution live-video feed camera, which provides a clear and magnified view of the microbots, which facilitates a real-time view, which is shown on a user's computer. This camera is placed above the arena and is placed perpendicular and centered amongst the magnetic probes. The camera is plugged into the user's computer over USB cabling, and shows the top-down view of the microbots.

The second part of our user interface involved the use of a physical controller in combination with the user's computer. To control our microbots, a computer that runs python is used as our central processing unit which allows our inputs from our physical controller to be translated into system outputs through a series of transforms. A regular computer was chosen over something such as a Raspberry Pi as it reduces costs and allows almost anyone to interface with the device as they can use their existing computer. Personal computers are also much more powerful than a Raspberry Pi and support the USB protocol with individually addressable peripherals, runs Python natively, has support for a communication baud rate of 9,600, and most of the time contain Bluetooth which allows us to communicate with our wireless controller.

Our physical controller which is connected via Bluetooth to the computer is used, as our inputs which are mapped to outputs in the system. An Xbox One Wireless Controller was chosen due to the familiarity of the controller, as well as its support for the controller drivers natively with Python. As we are using a six-coil design, six degrees of freedom are available for microbot control. The left joystick of the controller is used to control two degrees of freedom, being the x and y axis while the right was used for another degree of freedom being the angle to which our microbot faces. This takes advantage of three of our degrees of freedom but also leaves three

unused degrees of freedom. To address most of the customer requirements, the decision to only use three degrees of freedom for movement in x, y, and rotation was made, as this would accomplish 90% of the desired movement.

The next component in relation to the low-level system includes the magnetic field control module. In our 6-magnet system, the magnetic field control module serves as the critical component in effectively manipulating the microbot. It is responsible for interpreting user inputs and translating them into precise adjustments to the magnetic field. With software, the current flowing through each of the six electromagnets can be changed to generate a wide range of magnetic field shapes and gradients, which in turn enables a variety of microbot behaviors and orientations.

Using the signal from the computer, the driver circuit for each coil is amplified to a maximum voltage of 24V to 10,000 turns of 24 AWG copper wire. This spec of copper wire was chosen due to the resistance it provides ( $48 \Omega$ ), and the corresponding current of 500 mA. The entire winding has a cross section of 8 cm x 2.5 cm, which is thin enough to allow for power dissipation on all surfaces of the coil, helping reduce maximum internal temperature which had a power dissipation of 10 watts. The thickness of the coil and the heat sinking effect of the core, the 10 watts of power is managed with passive convective dissipation, however the use of computer grade fans are used as well. There are two fans, one inlet, and one outlet, to cycle the air through the machine. In series to each winding is a  $1 \Omega$  shunt resistor that is fed into the microcontroller's analog to digital converter, allowing current to be measured and back electric and magnetic fields in each coil are calculated. This provides an additional redundant layer of sensing for the magnetic flux in the outer cores.

To control the amount of current going through each coil, motor drivers were needed. We use three Pololu Dual G2 High-Power Motor Driver 18v22 Shield for Arduino. These motor drivers can control two motors/coils per board and therefore with three boards, we can control all 6 of our electromagnets. The Pololu motor drivers were chosen as they support a wide operating voltage between 6.5 V to 30 V which was useful when prototyping in case changes were needed. It also supplies up to 22 A of current which is much larger than needed. Lastly, the boards were designed specifically for use with an Arduino board such as the Teensy 4.1 and source code was provided to use them specifically.

The final component in relation to the low-level system is the communication and integration. The software interfaces with the hardware components, such as the array of electromagnets to control the magnetic field, and to get position inputs from our controller. The multiple components of our final design need to communicate with each other to complete such tasks. Communication between the remote controller and the computer occurs over Bluetooth. This was chosen to create an easy-to-use system without cables for our users to interface. Communication between the computer and the Teensy 4.1 occurs over USB cabling, as well as the connection between the microscope camera to the computer. The USB protocol was chosen for these connections over other protocols such as UART as it uses differential pairs to transport messages compared to UART which does not and can have electromagnetic interference in the form of data loss. All these connections use shielded USB cabling to further reduce electromagnetic interference and a baud rate of 9,600 bits per second was chosen as it is the most common baud rate which satisfies our data transfer needs and is supported by both the computer and Teensy 4.1. To communicate between the Teensy 4.1 and the Pololu Arduino shields, PWM is used. PWM is used as the signal remains digital from the Teensy

to the Pololu which reduces noise. It is also the most common communication protocol for use cases for motor controllers.

## Design Verification

### High Level

Given the plan mentioned above to include a control loop, an evaluation and iterative improvement method was developed. Once the prototype was built, the plan was to test its efficiency by tracking the time needed from a given set state to be reached, i.e. the number of iterations through the control system needed to fall below a 10% error of the required field. From there, the control system would be refined using real world data if necessary. While simulation data may have been able to rely on the Jiles-Atherton or circular model, errors inherent to the physical system could in theory result in model parameters to be tweaked. This includes but is not limited to the exact material properties of the steel probes and the wires. The steel simulated was hot rolled 1010 Steel, but the procured steel from the university may have slightly different hysteresis characteristics.

To verify our system's ability to generate our desired magnetic fields in the arena, COMSOL simulations were conducted and plotted in Appendix E. Note that these are simply screenshots of a running video simulation which shows the dynamic oscillation of the field. Several coil drive configurations were tested to characterise the transfer inductance of the system, as well as help identify deviations from expected fields. Coil configurations included dipoles, quadrupoles, hexapoles, as well as linear combinations of all configurations. In simulation, it was found that saturation of the cores was reached at around 10k Amp-turns. This would have led to undesirable hysteretic effects, which would have made controlling the system a more difficult task. The data obtained was therefore used to reduce the power output of the system.

Figures E.3, E.6, E.9, and onwards show the magnetic flux at various diameters within the arena. These results showed sharp peaks nearest to the probe tips, due to the sharp corners of the probes. In practice, these sharp oscillating peaks would be much smaller in amplitude, as the corners are not actually infinitely sharp. Also, in our physical prototype, we opted to use flat tips instead of angled as shown in the verification data. This was done because the function of the angled tips was to focus the magnetic flux at those areas. This was however not needed, as explained above.

To continue, we conducted lumped modelling calculations and established that a cooling system was not required for the electromagnets of our designed prototype. As high current DC current is running through our electromagnets for extended periods of time, we were anticipating a high amount of heat dissipation in our system due to joule heating of the wires. The original cooling design used hollow wires for concentric cooling. However, this greatly hindered the number of amp-turns and consequently achievable flux at the probe tips. The second iteration then involved a cooling channel to be machined into the cores with coolant circulating, as well as transformer oil in the space between coil windings to increase heat conductivity and heat dissipation. Neither of these systems were warranted based on our calculations. Resistance of 5000 amp-turns was calculated to be 70 ohms, giving 32 watts of heat to dissipate. With this estimate, as well as the high heat conductivity of the core, cooling in the form of fans was found to be sufficient.

### Low Level

For the low-level system, many parts of the system needed to be verified to ensure accuracy in our results. Although verification for the low-level system was less analytical, several tests were created. The main aspects of our verification plan included bottom level, integration, and end-to-

end testing of our system and components through a series of unit tests. Bottom level testing involved ensuring all components purchased such as microcontrollers and motor drivers worked and to ensure their accuracy. An example test included using the XBOX controller to verify all input values such as the joystick in different values and making sure that the computer interpreted those inputs correctly. The next stage of unit testing was integration testing which involved the testing of multiple parts that are integrated together. An example of this type of test for our system included sending commands to the microcontrollers and having them relay the commands back to the computer to ensure communication without data loss. The final type of testing for the low-level system included end-to-end testing which involves testing the system to ensure the communication and the most or all the components can work together. An example of this type of test included the simulation of a set of inputs from the XBOX controller and verifying that the microbots move to the correct location or rotate in the correct location. This is an end-to-end test as it involves all aspects of the system from input to the output. Further specific testing can be found under User-System Interface in Appendix C.

Section User-System Interface in Appendix C outlines some of our previous software system verification, which is still valid, however there is a difference with the use of an x-y coordinate system rather than one in a complex space. The coordinate system was updated to use a complex space as it is more versatile with libraries in python for our application which therefore extends to the verification, we conduct using a complex space.

For the low-level system, a smaller amount of verification data is available compared to other parts of this project. This is because this technology and integration of parts has been tried and proven

in the past and is very robust. All specifications of the parts for the low-level system are suitable for our project both in design and in practice. We did conduct simulations to verify that our prototype would work. Figure E.1 depicts the visualization software for the magnetic field magnitude based on the desired microbot position. The input software can control the desired location of the microbot with the use of the XBOX controller, and the resultant magnetic fields are visualized. This testing validated the control software written as the microbot simulated location was able to be simulated and controlled with high accuracy and intuitiveness as to how the controller would control and correlate the controls to microbot movement.

### Prototype Construction

The first step in prototype construction was the creation of the electromagnets. The cores of the electromagnet were the starting point of this process. Eight bars of hot-rolled steel with dimensions 1 ft x  $\frac{1}{2}$ " x  $\frac{3}{4}$ " were procured from the university, each of which measuring 25 inches in length. Detailed steps of the prototype building process are given in Appendix F. The bars we were taken to the Engineering Machine Shop and underwent steps to match the design specifications. This consisted of cutting the bars to the desired dimensions using the vertical and horizontal bandsaws, a Calcium Lime Rust (CLR)/phosphoric acid treatment to remove the magnetic oxide layer on the outer surface of the steel, and milling/belt sanding steps to fine-tune the dimensions of the steel.

The pieces were then attached to adjustable HDPE slots to form the geometry of our system. At this point, the outer bars were placed through a circular copper pipe and the winding jig was used to add the copper wiring, finalizing the structure of our electromagnets. The result of this can be

seen in Figure 4: Machined iron parts held together using machine cut HDPE (left). Coil windings added to the iron cores (right). below.



*Figure 4: Machined iron parts held together using machine cut HDPE (left). Coil windings added to the iron cores (right).*

From here, a wooden housing was constructed to store the electrical components of the system. It was built to match the hexagonal geometry for design consistency. For safety purposes and to allow us to do live demonstrations of our prototype, the electronics were stored in a compartment under the electromagnets.

The low-level system comprised two key components for the prototype: hardware and software. The hardware, as depicted in Figure 5, required power management for various components. A 24V power supply connected to a 120V AC wall outlet powered the motor drivers, while a buck converter stepped down the voltage to 5V for the Teensy 4.1 and fans. Motor drivers were connected to two electromagnet coils each for current control.



*Figure 5: Microbot controller hardware compartment and final prototype.*

Data connections involved a USB port installed on the device frame, which connected to the Teensy 4.1 for convenient interfacing and reprogramming. PWM was used to control coil power magnitude, and additional connections handled coil sleep, fault, and direction.

The low-level system's software ran on both the host computer and the Teensy 4.1. Python code on the host computer managed controller inputs and maps them to control vectors for input into the Teensy 4.1. The code paired with the Bluetooth XBOX controller, mapped inputs, and converted values before sending control vectors via USB to the Teensy 4.1.

The Teensy 4.1 code received control vectors and sent commands to the motor drivers. A communication port was opened to receive control vectors, which contained six numbers representing coil power magnitudes. The Teensy 4.1 would then send the new position to motor drivers to adjust coil currents. A modified Pololu library was used to support three boards and six coils simultaneously. The cycle of receiving and setting coil currents continued in this manner.

## Test Results

Table 1 highlights the major test results in relation to the customer requirements. For power output, there was a desired magnetic field strength of one tesla, however only 0.8 was achieved which led to a success level of 80%. For the customer requirement of locomotion, there was desired movement in x, y, and rotation. All three of these DOF were achieved and therefore had a success level of 100%. For the customer requirement of the control mechanism, there was a desired result of local control of the microbots with the use of a PID control loop. The PID control loop was never realized and therefore a success level of 75% was achieved as the microbots were still controllable. For the customer requirement of complex local control, there was a desired complex local control using five DOF, however only three were achieved which were x, y, and rotation. The two other degrees of freedom being the change in the surface area, and the change in aspect ratio were not achieved. As the three that were achieved were the most important, 75% success level was attained. Table 1 shows a demonstration of our magnetic controller rotating our microbot from positive to negative  $\theta$ , and vice versa.

Table 1: Low-level test results versus customer requirements.

Customer Requirement	Test Results	Success Level
<i>Power Output</i>	Desired: 1 T <i>Actual: 0.8 T</i>	80%
<i>Locomotion</i>	Desired: x, y, $\theta$ <i>Actual: x, y, <math>\theta</math></i>	100%
<i>Control Mechanism</i>	Desired: Local control w/ PID loop <i>Actual: Local control</i>	75%
<i>Complex Local Control</i>	Desired: Local control w/ 5 DOF <i>Actual: Local control w/ 3 DOF</i>	75%
<i>Biocompatibility</i>	Desired: Literature backed bio compatible materials in actuator Actual: Oil and metal based actuator	0%

### Deviations / Shortfalls

There were several deviations from the original design, as well as shortfalls in the delivery of certain customer requirements. To start, plans to integrate the up and down arrows on the controller to control the surface area of our microbot, which would use another degree of freedom, as well as the left and right arrows being used to control the aspect ratio of our microbot was not used. This would have left one degree of freedom to spare however the current design of our controller only implements the use of three degrees of freedom being movement in x, y, and rotation. Our current design does not implement the other three degrees of freedom we have access to due to time constraints and the complexity of integration.

Haptic feedback in the controller using controller vibrations was also part of the original design however this was not implemented, again due to time constraints. The haptic feedback would have been used to simulate obstacles the microbots encounter. This would have improved on the customer requirements for complex local control of the robots to which our consultant evaluated

our deliverable at 75%, as well as our control mechanism which was evaluated at the same level of completion.

Another deviation that we had was the use of a personal computer to send control vectors to the Teensy 4.1, rather than the Raspberry Pi we had designed for. We had actually originally designed for a personal computer to be used, but later switched to a Raspberry Pi, and then switched back. We made this decision as we wanted an easy way to display the live-video feed of the microbots which was not possible without the use of a laptop or monitor. This did not affect our customer requirements.

We had originally planned to use the UART communication protocol between the personal computer and the Teensy 4.1, however we switched to USB. UART was chosen as we had previous experience with this protocol with respect to previous programming, however this would pose problems with the high electromagnetic interference our cabling would experience which could potentially cause data loss. UART transmits messages using a high and low voltage representing a 1 and a 0. With electromagnetic interference, these voltages might change after being sent which would affect their reading from the Pololu motor drivers and potentially cause some bits to be flipped. The USB protocol uses differential pairs by using 2 separate voltage lines, with the difference between them acting as a 1 or a 0. This allows for voltage fluctuations to affect both voltages with the potential difference staying the same, allowing for the signal to be more robust in the conditions our system will be in. This did not affect our customer requirements.

Another deviation was the change in components from the ATmega32U4 to the Teensy 4.1. This change was made as the Teensy 4.1 was a component we already had on hand and fit all the criteria we needed. Another component change was removing the use of a USB hub to address the ATmega32U4s as we moved from using several of these boards to just the Teensy 4.1.

The final component of the low-level system which was not attained was the live-feedback loop system, also known as a PID control loop with non-linear hysteresis effects. The key element to this system was the use of Hall Effect sensors with saturation around 1T to measure the output flux at the corners of the outer hexagon to be used for feedback from every iron core of the electromagnets and inner probes. However, the only sensors on the market available to us were ALS31313-2000 Hall effect. Their saturation was around 0.2T, meaning they would occasionally saturate, but provide accurate feedback when in their operating region. Their placement was then modified to the tips of the inner probes, as the field at the tips would be less likely to saturate than near the coils of the electromagnets. Measurement of the output flux (to be converted to field) would then be measured and later compared to the expected magnetic potential, which would allow us to adjust our output to correct for these inconsistencies.

We ran into an issue where we could not read any data from the sensors. Although we made custom PCBs for the sensors and spent a significant amount of time getting them to work, they appeared to be locked by the manufacturer. With no way of unlocking them, we would have had to pivot to another sensor and create new PCBs, however this was not feasible given our time constraint. The tracking software that we had planned to do was also not complete. Due to issues with the microfabrication of our microbots, the tracking software could not be implemented that was

designed to track the location of the microbots within the arena. This would have further contributed to the PID loop as we could relay information on the physical locations and configurations of the microbots, to further correct them if they were not in the configuration set out by the desired configuration. This heavily impacted our customer requirement of our control mechanism of which our consultant listed that we met 75% of. This impacted this customer requirement as we could no longer adapt our magnetic response to correct for inconsistencies between the desired and actual magnetic fields.

For a qualitative inspection of the field, we opted to use magneto chromic film purchased from amazon and placed it above the arena. In later tests, we were able to confirm oscillating flux in the probes when a rotating quadrupole was applied.

## Actuators

### Design Description

The system includes a solution phase designed to enhance the diamagnetic aspect of the system. This solution is composed of magnetic ions and is buffered to 4 pH. While the paramagnetic component is much smaller, the diamagnetic aspect, along with an image of the robot, is visible in Appendix E. To meet the necessary customer specifications outlined in Appendix A, consisting of biocompatibility, locomotion, and complex control, the diamagnetic component should be inexpensive to produce, biocompatible, have a high aspect ratio, and low diamagnetic susceptibility. SU8 2100 is a suitable material that meets these requirements. One idea explored to improve the paramagnetic component is to use aluminum loaded SU8 2100, which can be adjusted by changing the loading percentage. In the final prototype, iron and bismuth filings were used in

oil droplets since the actuators were not ready in time which do not meet the biocompatibility requirement outlined in Appendix A.

## Design Verification

### *Solution Chemistry*

The robotics subsystem is composed of three interdependent sections, and their reliance on one another is detailed in the design verification section. Moving forward, the term "lithography system" will refer to the magnetic solution and microrobots.

The backbone of the subdomain is the magnetic solution chemistry and the Magneto-Archimedes principle. The magnetic solution is used to amplify the diamagnetic nature of the components of the robotic. The reason this is necessary is due to the diamagnetic components being significantly weaker compared to the paramagnetic components, making it the limiting factor of the subsystem. Magneto-Archimedes system treats magnetic field like a fluid, and a vacuum in the field caused by any component creates a diamagnetic force similar to a buoyant force in a fluid, hence the name Magneto-Archimedes principle. This approach makes it easy to account for the force generated by the presence of the robot in solution. The magnetic solution consists of magnetic ions in a buffered state. The pH of ions needs to be selected so that the robotic components are in solid phase, but the solution components are in the desired ion phase.

The design criteria of the solution have two components. The transition metal ion needs to have a high molar magnetic field, with counterion such as chlorides having high solubility. Simple salts are significantly easier to synthesize, making the system cheaper.

A few metals are magnetically active, and out of that the ideal ions would have a high molar magnetic susceptibility. The choice was made to choose iron and manganese salts due to their high magnetic susceptibility in all ion phases [6]. On average, the Manganese (II) salts have susceptibility of  $0.010 - 0.014$  cubic cm per mol. Iron (II) and (III) have ranges of  $0.013 - 0.015$  cubic cm / mol. Another consideration that needs to be accounted for is the pH of the solution. The pH of the solution must be that under which the preferred phase is the ionic phase. In the Appendix B, we discussed the conditions under which the ionic phase can be achieved. At the pH of about 4.5 or below and a potential about  $\pm 0.5$  V, Iron is present in Iron (II) phase. Iron (III) requires a higher potential and a lower pH, conditions that many other transition metals cannot sustain in solid phase. Manganese (II) is the dominant phase in the region that Iron (II) can exist in solution. This is deduced from the Pourbaix graph of Manganese which can be found in Appendix B, which shows the relationship of phase to potential and pH of the system. In practice Iron (II) salts are significantly easier to synthesize than internally in the team than manganese salts, making them a more attractive option.

In summary, the solution for Magneto-Archimedes enhancement of the diamagnetic component consists of Iron (II) salts.

#### *Diamagnetic Components*

The design criteria for the diamagnetic component are that the magnetic susceptibility must be minimized. The element that has the lowest magnetic susceptibility is Bismuth [7], however, there are several practical reasons that make use of Bismuth as a diamagnetically component problematic. Bismuth is a difficult metal to deposit and electroplate, making the creation of robots

difficult as discussed in Appendix B. Electroplating is not viable option for Bismuth deposition, and chemical deposition is not a route that we would want to take due to difficulty controlling deposition quality and depth of deposition. Alternative options are polystyrene and SU-8. Polystyrene is easier and cheaper to create. It can be easily dissolved in acetone, and a spin coater can be used for deposition. However, the problem for polystyrene is mainly etching. Which can be solved using SU-8, making it a more practical choice. SU-8 is a photoresist has desirable magnetic permeability of 1.08 [8] that can be spun coated down to less than 100 um thickness easily [9]. The process flow of the SU-8 development is also well established, and it is a consumable that is extremely common in most labs. The biggest benefit for using SU-8 is that development of the resist can be done using masks that we are able to print, allowing us to cut down the costs of development significantly by avoiding the clean room and mask production. In summary, SU-8 would be the ideal diamagnetic component mainly due to the practical reasons such as ease of production. An alternative to SU8 diamagnetic layer is the using some use of baby oil or mineral oil. The oil is like SU8 in terms of diamagnetism, allowing for creation of diamagnetic bubbles.

### *Paramagnetic Components*

The paramagnetic components have three design criteria that need to be met. The paramagnetic material should have high susceptibility, should have the ability to be easily electroplated, and should exist in the solid phase at the pH and potential of the solution. The first design criteria limit the possible transition metals, and the only viable options are nickel, cobalt, and chromium. Chromium plating process is highly toxic and electroplating chromium is not a viable option due to its carcinogenicity [12]. Cobalt is completely in ionic phase in the region of interest [13]. This

leaves nickel, and it is at the very edge of the region where iron and manganese are ions, but nickel is in the metal phase. This makes nickel the only metal that meets all the criteria. There are other weaker options such as Aluminum [19] which have significantly lower but should be explored as well since stability criteria needs to be evaluated for each metal individually. For increased stability, the components can also be incorporated into SU8 to create a loaded SU8 section that is magnetically active.

### *Stability Criteria*

The stability criteria can be derived analytically. This method is superior to simulated verification due to the simplicity of this approach. The stability criteria can be found below in Equation 1: Stability Criteria and in Appendix E.

$$\mathbf{F} = \nabla(\mathbf{m} \cdot \mathbf{B}) \text{ and } \boldsymbol{\tau} = \mathbf{m} \times \mathbf{B} = 0$$

Since  $\mathbf{B} = \mu \mathbf{H}$  and  $\mathbf{m} = \chi \mathbf{H}$ , We can say that  $\mathbf{m} = \frac{\chi}{\mu} \mathbf{B}$

$$\text{Giving us } \mathbf{F} = \frac{\chi}{\mu} \nabla(\mathbf{B} \cdot \mathbf{B}) = \mathbf{k} \nabla |\mathbf{B}|^2$$

Treating  $\mathbf{B}$  as complex unit with  $n$  poles leads to  $\mathbf{B} = \mathbf{R}^{(n-1)} \cdot \exp[(n-1)\pi i\theta] = \mathbf{R}$

$\mathbf{R}$  is to the power of  $(n-1)$  since we need at least 2 poles

$$\mathbf{F} = \mathbf{k} \nabla |\mathbf{B}|^2 = \mathbf{k} \nabla |\mathbf{R}|^{2(n-1)} = \mathbf{k}(2n-2)(\mathbf{R}^{(n-1)})$$

$$|\mathbf{F}_D| = |\mathbf{F}_P|$$

Lets say  $\mathbf{R}_D, \mathbf{l}$  is the center of mass of diamagnetic and length so

$$\mathbf{k}_D \nabla |\mathbf{R}|^{2(n-1)} = \mathbf{k}_P \nabla |\mathbf{R} + \mathbf{l}|^{2(n-1)} \text{ which leads to}$$

$$R = \frac{l}{\sqrt[n-1]{\frac{k_p}{k_D} - 1}} \text{ where } k_D > k_p \text{ for the system to be stable}$$

*Equation 1: Stability Criteria*

To determine the right paramagnetic component thickness, the Equation 2: Paramagnetic Thickness can be leveraged which can also be found. With the desired thickness of 400 um of diamagnetic layer, thickness of 0.17 nm if we use the values of 600 for Nickel [10] and -1.66e-4 for Bismuth [7]. By using Aluminum, we can achieve a thickness of 288 um since the value for Aluminum is 2.2e-5 [11].

$$t_{paramagnet} = \frac{400(-2\chi_{Bismuth})}{1.3(\chi_{paramagnet} - 2\chi_{Bismuth})} \mu m$$

*Equation 2: Paramagnetic Thickness*

#### Actuator Prototype Construction

Because of limited funds, it was decided to attempt producing the actuators in Dr. Hamed Shahsavan's laboratory, where a spin coater is available. The sacrificial layer employed is Brilliant Yellow, which dissolves in water. An Epoxy layer is first spin coated and soft baked, followed by another Epoxy layer that is spin coated and filled with Aluminum. A laser printer is used to create the mask, which is then transferred via contact printing. Refer to Figure 6 below for a visual representation of this procedure. The details test procedure can be found in Appendix D.

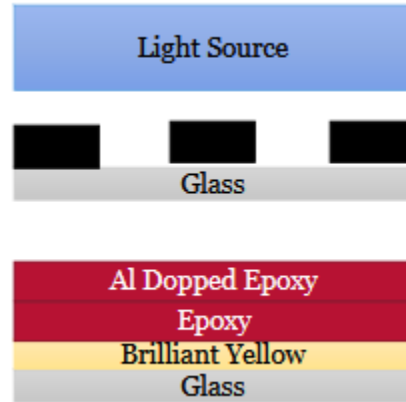


*Figure 6: Thin Film Structure of actuator*

Acquiring SU8 2100 proved difficult, so a DLP resin was substituted for the epoxy layer instead. The decision to use this resin was based on its ability to cure at a 405 nm wavelength, which could be produced by a lab lamp, and its affordability. However, after several tries, the DLP resin was discarded as it caused the sacrificial layer to dissolve. In

Figure 7, this issue is demonstrated by the DLP resin beading up and dissolving the sacrificial layer within.



*Figure 7: Beading of DLP Resin*

SU8 2100 was obtained from IDEATION lab and the process was repeated with SU8 2100 being the epoxy layer. Protocols on the manufacturer website were followed, however, transferring of

the pattern onto SU8 could not happen. Figure 8 shows the lack of pattern and cracks forming in developed SU8.



*Figure 8: Issue with Pattern Transferring Onto SU8*

Ultimately, the actuator design had to adopt the oil-based approach, which was briefly referenced in the design verification section. The primary reason for this decision was the straightforwardness of the bead, which comprised of a blend of baby oil, Iron, and Bismuth filings. The beads were inserted between an organic layer of isopropyl alcohol and a solution layer of saturated Iron (II) Chloride. Figure 9 below illustrates the setup of the system. The detailed synthesis for the solution and the oil-based actuators can be found in Appendix D.

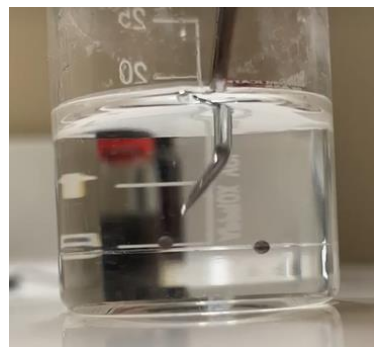


*Figure 9: Oil Bead Actuators*

## Test Results

The testing of actuators was mainly qualitative, with the testing consisting of whether certain actuations were possible. With the system, we were able to test out that actuations with high degrees of freedom were possible. Table of test results can be found in Appendix F.

The actuators were able to rotate and move in x-y plane. This partially met the customer requirement of at least 2 degrees of freedom with ideally 5 degrees of freedom for the first prototype. The actuators were also able to move over a total absolute distance of 2 cm using the degrees of freedom available, meeting the customer requirement of locomotion of the actuators. Biocompatibility requirement was abandoned halfway through the project due to logistical and experimental issues with fabrication of actuators. The final version is not biocompatible due to the large oil based diamagnetic component that is part of it [12].

Table 2: Customer Requirements for Actuators

Customer Requirement	Test Results	Success Level
<i>Locomotion</i>	Desired: $x, y, \theta$ <i>Actual: <math>x, y, \theta</math></i>	100%
<i>Biocompatibility</i>	Desired: Literature backed bio compatible materials in actuator <i>Actual: Oil and metal based actuator not found to be safe inside body [12]</i>	0%
<i>Complex Local Control</i>	Desired: Local control w/ 5 DOF <i>Actual: Local control w/ 3 DOF</i>	75%

### Deviations and Shortfalls

The primary departure from the original design involved substituting epoxy actuators with oil beads. The rationale for this deviation was thoroughly discussed during the prototype construction phase of the actuators. Despite the ambitious decision to construct the actuators in a non-cleanroom setting, contingency plans were devised in anticipation of potential development setbacks. Meeting the customer's biocompatibility specifications, as mentioned in Appendix A, hinged on creating small actuators from materials that wouldn't seep into the body or trigger an immune response. This is why SU8, which can be rendered biocompatible, was utilized [13]. However, the final version of the actuator failed to fulfill the requirements due to its relatively large size and use of oil-based diamagnetic components. The group members viewed the deviation as necessary to emphasize the novelty of the control system.

### Summary

The main objective of the microrobots is to allow precise and observable control over the locomotion of microbots in an arena. To achieve this, the project has been divided into 3 subtasks. The first is concerned with the development of control software, followed by the construction, and mounting of a physical controller, and finally fabricating and controlling the actuators.

The first section, which consists of the translation of user input to a signal for current needed in each coil, defines the control system. The steps have been outlined as follows. The inputs define a desired configuration of a magnetic field in the arena. This field is then defined at the boundaries as the superposition of 6 basis vectors at the MagneToad tips. The main task of the control system is to produce the desired fields while accounting for the nonlinear relationship between field and magnetizing force. This relationship is given both by hysteresis and saturation. The first issue is partially addressed by having accounting for the hysteretic behaviour through the Jiles-Atherton model, as well as the application of AC demagnetization to bring the curve back to its an hysteretic line. Saturation effects are both addressed via error feedback, as well as the fact that operation is limited to well under saturation point. The magnetizing force necessary is given by its relationship to Ampere's current law, which serves as input to the low-level components of the system.

In terms of high-level system progress, the main components of the system have already been purchased, with some parts awaiting delivery. The build procedures have been prepared, with minor to no tweaks anticipated other than the addition of control system tweaking once real data is achieved. Next steps include machining the parts, attaching the windings, and mounting the magnetic system. Verification steps of the models already prepared will rely on the completion of the lower-level mounting of the system. With that, the customer requirements relating to the control system, namely the mapping of user input to the physical controller, are expected to be met and optimized for the set deadline of March 17th.

The objective of the low-level system is to create a way to visualize, track and control the robots with the assistance of a live feedback loop using the magnetic parameters of the system. This

involves the use of user input in the form of an Xbox One Controller to feed in coordinate commands which will be used to control the robot. The aim is to have an intuitive user-interface with a live magnified video feed of the arena displayed on a screen.

An overview of the current progress with respect to the low-level system includes ordering of almost all parts as well as the preliminary prototype construction of the computer hardware and input system. This involves the setup of the Raspberry Pi with the latest version of Raspbian OS along with software such as Visual Studio code and it being linked to our team GitHub repository. Several programs have already been written with respect to pairing and taking inputs from the Xbox One Controller.

The future outlook in this domain seems positive with the next stage including setting up and verifying the Hall effect sensors and microcontrollers to start our feedback loop. This will involve making connections over USB to the microcontrollers and creating software to enable communication between the parts however this is all manageable. We have a high level of confidence that we will be able to meet our customer requirements for the low-level subsystem (namely the electrical and software systems by March 17th. This is because we are currently on schedule, which is shown in Appendix B. There are currently no further anticipated problems other than the minor ones discussed in the Encountered Issues and Plans to Address Them, section under the low-level Discussion. Although it is hard to predict future issues that may come up, much of the technology of the low-level section of this project has been used before from several team members during Coops or during personal project.

Finally, from perspective of the microbot actuators, there are three working components with the paramagnet, diamagnet, and solution chemistry. The largest challenge of the system is the fabrication in a cost-effective manner while meeting customer requirements.

The system of actuators uses a solution phase to enhance the diamagnetic aspect of the system. The solution is composed of magnetic ions and is buffered to 4 pH. The diamagnetic component should be inexpensive to produce, have a high aspect ratio, and low diamagnetic susceptibility. Iron (II) salts are used in the solution, which is buffered to a pH range of 3.6 to 4.5. The design criteria for the diamagnetic component is that the magnetic susceptibility must be minimized, and SU-8 is a suitable material that meets these requirements. However, due to unexpected failures in the fabrication of the actuators, the plan was pivoted to an alternative actuator which is not biocompatible. The actuators fabricated in the end consist of oil phase with particles of iron and bismuth in this.

## References

- [1] O. Baun and P. Blümller, "Permanent magnet system to guide superparamagnetic particles," *Journal of Magnetism and Magnetic Materials*, vol. 439, pp. 294-304, 2017.
- [2] B. Shapiro, "Towards dynamic control of magnetic fields to focus magnetic carriers to targets deep inside the body.," *Journal of magnetism and magnetic materials*, vol. 321, no. 0304-8853, p. 1594, 2009.
- [3] X. Hui, S. Mengmeng, F. Xinjian and C. Weinan, "Reconfigurable magnetic microrobot swarm: Multimode transformation, locomotion, and manipulation," *Science Robotics*, vol. 4, 2019.
- [4] C. Xin, D. Jin, Y. Hu, R. Li, L. Wang, Z. Ren, D. Wang, S. Ji, K. Hu, D. Pan, H. Wu, W. Zhu, Z. Shen, Y. Wang and J. Li, "Environmentally Adaptive Shape-Morphing Microrobots for Localized Cancer Cell Treatment," *ACS Nano*, vol. 15, no. 11, 2021.
- [5] D. C. Jiles and D. L. Atherton, "Theory of ferromagnetic hysteresis (invited)," *Journal of Applied Physics*, vol. 55, no. 6, pp. 2115-2120, 1984.
- [6] "MAGNETIC SUSCEPTIBILITY OF THE ELEMENTS AND INORGANIC COMPOUNDS," [Online]. Available: <http://www.fizika.si/magnetism/MagSusceptibilities.pdf>.
- [7] S. Otake, M. Momiuchi and N. Matsuno, "Temperature Dependence of the Magnetic Susceptibility of Bismuth," *Journal of the Physical Society of Japan*, vol. 49, pp. 1824-1828, 1980.
- [8] MIT, "MIT Material Property Database," MIT, [Online]. Available: <http://www.mit.edu/~6.777/matprops/su-8.htm>.
- [9] KayakuAM, "SU-8 2000 Permanent Negative Epoxy Photoresist," KayakuAM, August 2020. [Online]. Available: <https://kayakuam.com/wp-content/uploads/2020/08/KAM-SU-8-2000-2025-2075-Datasheet.8.19.20-final.pdf>.
- [10] J. F. Schenck, "The role of magnetic susceptibility in magnetic resonance imaging: MRI magnetic compatibility of the first and second kinds," *Medical Physics*, vol. 23, no. 6, pp. 815-850, 1996.
- [11] Georgia State University, "Magnetic Susceptibilities of Paramagnetic and Diamagnetic Materials at 20°C," Georgia State University, [Online]. Available: <http://hyperphysics.phy-astr.gsu.edu/hbase/Tables/magprop.html>.
- [12] IARC Working Group on the Evaluation of Carcinogenic Risks to Humans, Chemical Agents and Related Occupations., Lyon (FR): International Agency for Research on Cancer, 2012.
- [13] Z. Chen and J.-B. Lee, "Biocompatibility of SU-8 and Its Biomedical Device Applications," *Micromachines (Basel)*, vol. 12, no. 7, p. 794, 4 Jul 2021.
- [14] F. Rumiche, E. Indacochea and M. Wang, "Assessment of the Effect of Microstructure on the Magnetic Behaviour of Structural Carbon Steels Using an Electromagnetic Sensor," *Journal of Materials Engineering and Performance*, vol. 17, pp. 586-593, 2008.
- [15] michrochem, "SU-8 2000 - Permanent Epoxy Negative Photoresist - PROCESSING GUIDELINES FOR SU-8 2100 and SU-8 2150," [Online]. Available:

- <https://kayakuam.com/wp-content/uploads/2019/09/SU-82000DataSheet2100and2150Ver5.pdf>.
- [16] T. P. Man, "G-Bioscience," G-Bioscience, 13 May 2014. [Online]. Available: <https://info.gbiosciences.com/blog/bid/197554/biological-buffers-ph-range-and-how-to-prepare-them>.
- [17] The Northeast Waste Management Officials' Association, "Pollution Prevention Technology Profile: Trivalent Chromium Replacements for Hexavalent Chromium Plating," The Northeast Waste Management Officials' Association, 18 November 2003. [Online]. Available: <https://www.newmoa.org/prevention/p2tech/TriChromeFinal.pdf>.
- [18] E. M. Garcia, J. S. Santos, E. C. Pereira and B. J. G. F. M., "Electrodeposition of cobalt from spent Li-ion battery cathodes by the electrochemistry quartz crystal microbalance technique," *Journal of Power Sources*, vol. 185, no. 1, pp. 549-553, 2008.
- [19] CACF, "Nickel Electroplating," CACF, [Online]. Available: <https://www.casf.ca/wp-content/uploads/2014/04/NickelElectroplating.pdf>.
- [20] B. C. Johnson, "Electrical resistivity of copper and nickel thin-film interconnections," *Journal of Applied Physics*, vol. 67, no. 6, pp. 3018-3024, 1990.
- [21] J. Moran--Mirabal, "PIRANHA CLEANING – GLASS SURFACES - Chemistry McMaster," May 2014. [Online]. Available: <https://www.chemistry.mcmaster.ca/moran-mirabal/resources/PIRANHA-CLEAN-5-2014.pdf>.
- [22] Shimadzu, "Cleaning Procedure for MALDI sample targets," Shimadzu, [Online]. Available: <https://www.shimadzu.eu.com/cleaning-procedure-maldi-sample-targets>.

## Appendices

### Appendix A

#### *Customer Requirements*

The two applications that the system can be applied to are minimally invasive surgery, and targeted drug delivery. The overall customer requirements consider the services provided by the competitors, the general trends, and specific needs expressed either in literature or through interview. Table A.1 can be found below.

*Table A.1: Summary of Customer Requirements*

<b>Requirement</b>	<b>Type</b>	<b>Functionality</b>	<b>Minimum Requirement</b>
Biocompatibility	Primary	Functional	Robots Must include materials used in other FDA approved products
Power Output	Primary	Functional	About 1 Tesla of Magnetic Field generated
Locomotion	Primary	Functional	Move the robot 2 cm
Control Mechanism	Primary	Functional	Centimeter level precision
Heating (Safety)	Secondary	Non-Functional	Coil temperature must not exceed 100 °C
Complex local control	Secondary	Functional	Robots must be actuated with at least 2 local degrees of freedom.
Control Mechanism (Stringent Requirement)	Secondary	Functional	Millimetre level precision

#### *Minimally Invasive Surgery (MIS)*

The proposed system allows for final control group of microbots, a feature that can be exploited for minimally invasive surgeries. The proposed application can also be found in literature for ideas which is explored in-depth in similar technology subsection. Key surgeries that require MIS technology are cardiothoracic surgery, gastrointestinal surgery, orthopedic surgery, gynecological surgery, cosmetic & bariatric surgery, and urological surgery [A.1].

MIS is projected to grow upwards of 28.9 billion USD in US alone by 2026 with a projected yearly growth of 7.4% [A.1]. This specific subfield is in a unique position of demand at the covid-19 pandemic. Massive backlogs due to diversion of resources are leading to a surgery crisis. Getting rid of the backlog will take a long time as there is 25 months (about 2 years) of wait time for cataract surgery in Ontario as of November 2021 [A.2]. The use of minimally invasive robots can decrease recovery times for patients, leading to more resources being used to overcome.

Worldwide, the demand for surgeries is immense as well. World Health Organization (WHO) in 2019 estimated that there are about 235 million major surgical procedures every year [A.1]. Growing senior population and growing access to healthcare around the world is going to increase the need for surgery in the future. Furthermore, the Association of American Medical Colleges projects that by 2034, there may be a shortage of between 15,800 and 30,200 physicians specialized in several types of surgeries [A.3]. This presents a perfect opportunity for an MIS product of the sorts being developed by us.

Regulatory constraints are present, especially in developed countries such as US and Canada [A.1] and may be a future hurdle that needs to be handled from now. “Power, biocompatibility, localization and locomotion” are key medical issues that need to be addressed by MIS robots and present topics for future research.

### Similar Technologies

Several MIS technologies are currently in use in the medical field. Two of the commonly used MIS technologies are robot assisted surgery, and capsule endoscopy [A.4]. Robot assisted surgery relies on large scale, high precision robots. Companies that are currently researching this subfield of MIS include Intuitive Surgical, Johnson and Johnson, Medtronic, and Stryker [A.5].

Specifically, in the subfield of GI surgeries, capsule endoscopy is an alternative minimally invasive diagnosis method.

### [Interviews](#)

As part of our customer review, we contacted researchers and doctors specializing in several forms for surgery. One of the interviews was with Dr. Lazar Klein, Gastrointestinal (GI) surgeon and researcher at University of Toronto. Dr. Klein was interested in the technology being developed due to its possible future applications. Dr. Klein believed that this technology could potentially be used for areas that are difficult to reach using traditional methods (such as surgery around that heart). Dr. Klein also showed interest in a future variation where parts could be inserted into the body in a minimally invasive manner and have them assemble into magnetically controllable surgical equipment inside the body.

### [\*Targeted Drug Delivery\*](#)

Targeted drug delivery systems are extremely useful, especially for the illnesses such as cancer. The industry is expected to grow at a rate of 15% with current valuation of the global targeted drug delivery being at approximately 6 billion USD [A.6]. This is part of a larger global trend of personalized healthcare product with an approximate global valuation of approximately 500 billion USD [A.7]. Several classes of illnesses can be selectively targeted using drug delivery systems, and include Cardiovascular Diseases, Pulmonary Diseases, and Oncological Disorders [A.6] with the main competitors being AbbVie, Sanofi, Janssen, and Roche.

### [Similar Technologies](#)

Nanoparticles are currently a topic of interest in the field of drug delivery. Polymer based nanoparticles are used extensively in research for delivery of both traditional molecule-based

medication and siRNA-based medication [A.8]. Surface functional groups are used to ensure the drug is targeted and cause low amount of collateral damage [A.8]. Furthermore, magnetic nanoparticles have also been employed in targeted drug delivery due to their top-down control property [A.9].

#### *Primary Requirements*

- Biocompatibility
  - o Biocompatibility is an important component of any system that interacts with humans. Selection of material that is biocompatible and can be removed by the body is an important limiting factor.
    - All the products used in microrobots must already be used in other FDA approved material to some capacity.
- Power output
  - o The system must be able to generate enough power for useful tasks. Proof of concept design must focus on getting maximum power output on the magnetic bubbles.
    - The maximum magnetic field strength we can achieve with iron is about 1 Tesla.
- Locomotion
  - o The microbots must be able to move from one location to another for the application. This is one of the fundamental requirements of the system.
    - The system must be able to move the microrobot over 2 cm.
- Control mechanisms

- Targeted control mechanism is the key part of this technology. The system must demonstrate the ability to control magnetic bubbles with high precision and being able to deliver them to target of interest.
  - Proof of concept prototype must achieve a centimeter level precision.

*Secondary Customer Requirements*

- Heating System (Safety)
  - The coils can heat up and pose a danger to users and the end customers. Maximum safe temperature needs to be established to ensure the safety of the users.
    - The system must not heat above 100 °C.
- Multiple degrees of freedom
  - In both drug delivery and surgery environments, robot must be able to move in different directions and be able to achieve higher degrees of freedom for any useful task.
    - The system must achieve 2 degrees of local freedom.
- Control mechanisms (Stringent)
  - The microrobots would be working in high precision environments inside the body and precision is extremely important.
    - The system should achieve a millimeter level precision.

## References

- [A.1] "Minimally Invasive Surgical Instruments Market by Product (Handheld Instruments, Inflation Devices, Surgical Scopes), Type of Surgery (Cardiothoracic, Gastrointestinal, Orthopedic, Urological), End User (Hospitals, ASCs), Region (2022 - 2026)," MarketsandMarkets, September 2021. [Online]. Available: [https://www.marketsandmarkets.com/Market-Reports/minimally-invasive-surgical-instruments-devices-market-682.html?gclid=CjwKCAiAn5uOBhADEiwA\\_pZwcP4D286lI2gO6-BSNgdvpUWaOGBfz2aopZ9aC8n2eO5XeAMjP-ZaPRoCLDwQAvD\\_BwE](https://www.marketsandmarkets.com/Market-Reports/minimally-invasive-surgical-instruments-devices-market-682.html?gclid=CjwKCAiAn5uOBhADEiwA_pZwcP4D286lI2gO6-BSNgdvpUWaOGBfz2aopZ9aC8n2eO5XeAMjP-ZaPRoCLDwQAvD_BwE). [Accessed 19 09 2022].
- [A.2] C. Lieberman, "Ontario hospitals tackle 'staggering' surgical backlog caused by COVID-19," Global News, 18 November 2021. [Online]. Available: <https://globalnews.ca/news/8384158/ontario-hospitals-tackle-surgical-backlog/>. [Accessed 19 09 2022].
- [A.3] "AAMC Report Reinforces Mounting Physician Shortage," AAMC, 11 June 2021. [Online]. Available: <https://www.aamc.org/news-insights/press-releases/aamc-report-reinforces-mounting-physician-shortage>. [Accessed 19 09 2022].
- [A.4] N. Simaan, R. Yasin and L. Wang, "Medical Technologies and Challenges of Robot-Assisted Minimally Invasive Intervention and Diagnostics," *Annual Review of Control, Robotics, and Autonomous Systems*, vol. 1, no. 1, pp. 465-490, 2018.
- [A.5] "Top 8 Robotic Surgery Companies in the United States," iData Research, 8 August 2022. [Online]. Available: <https://idataresearch.com/top-robotic-surgery-companies-in-the-united-states/>. [Accessed 19 09 2022].
- [A.6] "Global Targeted Drug Delivery Market to Surpass US\$ 22,704 Million by 2030, Says Coherent Market Insights (CMI)," COHERENT MARKET INSIGHTS, 22 April 2022. [Online]. Available: <https://www.globenewswire.com/news-release/2022/04/22/2427377/0/en/Global-Targeted-Drug-Delivery-Market-to-Surpass-US-22-704-Million-by-2030-Says-Coherent-Market-Insights-CMI.html>. [Accessed 19 09 2022].
- [A.7] "Personalized Medicine Market Size, Share & Trends Analysis Report By Product (Personalized Medical Care, Personalized Nutrition & Wellness, DTC Diagnostics, Telemedicine, Complementary Medicine), And Segment Forecasts, 2021 - 2028," Grand View Research, [Online]. Available: <https://www.grandviewresearch.com/industry-analysis/personalized-medicine-market>. [Accessed 19 09 2022].
- [A.8] C.-M. Hu, S. Aryal and L. Zhang, "Nanoparticle-assisted combination therapies for effective cancer treatment," *Therapeutic delivery*, vol. 1, pp. 323-334, 2010.
- [A.9] O. Veiseh, J. Gunn and M. Zhang, "Design and fabrication of magnetic nanoparticles for targeted drug delivery and imaging," *Advanced Drug Delivery Reviews*, vol. 62, no. 3, pp. 284-304, 2010.

## Appendix B

### Verification Plan

#### *Controller Tuning and Verification*

Within the arena, the magnetic field is completely described by its boundary conditions. This allows us to determine the magnetic field across the arena by simply measuring it along its boundary. To perform this measurement, we will use a ring of 6 three-axis hall effect sensors. The z-axis of these sensors will help us validate that the magnetic system is level, while the other axes measure the normal and tangential field. Validation of the sensor ring's accuracy will be conducted using magnetic viewing films.

The iron lens of the system provides the largest challenge to accurate control. Out of cost, we are restricted to using materials with high magnetic hysteresis, which is difficult to control over space. Although models for magnetic hysteresis do exist, the problem can be bypassed entirely by superimposing an ac signal over our control signal. This ac signal creates a demagnetizing field, which dissipates hysteretic magnetization to heat in the ring. The resulting B-H relationship is anhysteretic and depends on material parameters.

Optimal dissipation occurs when the drive voltage and back-EMF in the coils are  $90^\circ$  out of phase, which we can use to tune the ac signal's frequency. As the ac signal exists to correct hysteresis error, its amplitude will be proportional to the hysteresis error for each coil. This proportionality factor, as well as the material parameters, will be determined through tuning the system with the sensor ring and viewing film.

#### *Coil Simulations*

Simulation of the coil will be among the crucial components needed to have a functioning controller. Input parameters will be current supplied to the coil, desired functioning temperature

of the coil, wire dimensions and coolant choice. The outputs will be the magnetic flux  $\Phi$  through the central cores and the coolant flow rate needed to maintain a certain coil temperature.

The first step will be solving the necessary differential equations needed to obtain some desired magnetic field  $\mathbf{B}$ . The Biot-Savart Law can be used to obtain the field through a 1 layered inductor, and can be integrated over the number of layers/coil thickness to get the overall  $\mathbf{B}$ . The next and final step will be to measure magnetic flux through the iron core, i.e., dividing by the magnetic reluctance of the core. These calculations will be used to determine the amount of wire needed. These steps will be repeated for 2 designs (densely packed and hollow coils).

As coil heating is anticipated, the cooling mechanism through the two designs will be evaluated. Analytically, the packed coils can be approximated as a single heating block to be cooled at the outer and inner (between coil and core) interfaces, with coolant flowing in parallel w.r.t. the heated interface of the block. Inlets and outlets will be situated along the circumference of the coils on both ends. The second design will consist of concentric flow through the coil wire where the outer interface of a certain thickness is circumferentially heated. This heating can be calculated using the transient energy balance equation below:

$$\rho C \frac{\partial T}{\partial t} + \nabla \cdot (-k \nabla T) - Q_{cool} = 0 \quad Q_{cool} = \frac{dm}{dt} \frac{C(T_{inlet} - T)}{2\pi RS}$$

Where  $T$ ,  $\rho$ ,  $C$ ,  $k$  are temperature, density and specific heat of the coil, and thermal conductivity, respectively.  $Q_{cool}$  is the heat loss due to circulating coolant, where  $dm/dt$  is the mass flow rate of the coolant,  $C$  is the specific heat of the coolant,  $T_{inlet}$  is the temperature of the coolant upon entry into the coil,  $R$  is the radius of the solenoid and  $S$  is the cross-sectional area of the channel through which the coolant flows.

From here, simulation tools will be used to model the parts we will build. Specifically, the parameters defined above will guide the design of the coils on Solidworks, and the parts will then be imported to COMSOL or ANSIS for Multiphysics simulations. The first of two main studies to be conducted will be the joule heating of the wires as the main source of power dissipation. Fluid flow in the system will be the second study, with coolant flow rate as input parameter. This design is likely to be eliminated at the simulation stage if the cooling of the first design is sufficient and the magnetic field produced is too weak. Nevertheless, this design will have the same output as the first, namely the temperature of the system given a certain flow rate. From the data to be gathered, one can then solve for flow rate needed for a given coil temperature, which will be the input and output parameters for this section.

Finally, the studies can be integrated: Given the desired working temperature and input current, the simulation will output the resulting magnetic flux and mass flow rate required for the system. This information will be used by the micro-controller to control the  $\mu$ -bots.

#### *Microrobot Verification*

Through a thorough literature review and analytical methods, the verification of the Solution Chemistry paragraph was conducted. This included examining the design criteria of the magnetic solution chemistry and the Magneto-Archimedes principle, as well as the selection of the diamagnetic component as seen in Appendix E where Pourbaix diagrams can be found for all relevant components in the model. The ideal transition metal ions were chosen based on their high molar magnetic susceptibility and solubility, with Iron (II) salts being the most practical option. The molar magnetic strength of the Iron (II) salts can be found in literature [14]. For the diamagnetic component, Bismuth was initially considered due to its low magnetic susceptibility

[7] but practical limitations led to the selection of SU-8 as the ideal option, which was confirmed through a review of its magnetic permeability and ease of production [10]. The use of baby oil or mineral oil as an alternative to SU-8 was also discussed. Analytical methods were also used for verification, with the stability and thickness equations to be found in Appendix E equations 1 and 2.

## Appendix C

### Test Plan for the Constructed Design Prototype

#### *User-System Interface*

To test the constructed design prototype with respect to the user-system interface, testing of the live-video feed, computer application, and the degrees of freedom of the microbot need to be conducted. To ensure that movement between the microbot and visual computer application occurs in real-time, there needs to be less than a 100-millisecond video delay between the camera and the computer application. To achieve this, another camera recording at 240fps will be used to record the arena and computer screen. A marker will be inserted into the arena and the number of frames that pass between the time the marker was shown to the arena camera and displayed on the computer screen will be assessed and required to be 24 frames or under to fulfill the requirement of having a video delay below 100 milliseconds.

To test our degrees of freedom, set parameters may be entered or our joystick controller may be used to manually alter the microbot in real-time. The grid on the bottom of the arena will be used as verification for movement in our degrees of freedom. The microbot will move with a constant velocity dependent on the actuated value from the joystick. For the x and y axes, tilting of the joystick between 0 and 30 degrees will lead to a linear increase in velocity from 0 to 20 um/s. Rotating the joystick should rotate the microbot at the same speed and angle. Buttons for increasing and decreasing surface area will alter the microbot at a set velocity. The same process occurs for changing the aspect ratio to a skinnier or rounder shape. Simulating these values will be entered into the controller software where movement will be tracked with the camera system and the grid markers on the arena to verify speed by calculating distance travelled over time. Our tolerance is within 10% of our desired throughput and therefore a successful test result will need to be within this tolerance.

## *Magnetic System*

As the magnetic system is particularly complex, we anticipate that some iterative design may be required. Fortunately, this iterative design is only for the driving software of the robot, and no assembly or fabrication is needed between iterations.

Magnetic field data will be acquired through a combination of the hall effect sensor ring, and a sheet of magnetic viewing film under the arena. The sensor ring will give one depiction of the field in the arena through its boundary conditions, and the viewing film will give us another independent depiction of the field through the geometry of its nodes. Both depictions can be used together for a complete picture of the magnetic field. With our system, we wish to be able to control the field to within 10% RMSE across the arena.

This is a first prototype; we are anticipating that some error in the control system will persist into demonstration. Error is likely to show through specific distortions in the measured field. We accept these distortions, so long as they don't significantly affect the controlled DOFs (<10% relative error) or change the actuator array's topology (isomorphic to the circle).

Model training and evaluation is essential to having a predictable and repeatable system. Training will start by attempting to fit the anhysteretic Jiles-Atherton model to magnetization data acquired from our controller. Similar models which are faster and more numerically stable will also be fit and compared. The simplest model that describes the data with less than 1% RMSE will be used, with cubic splines as a fallback.

### *Coil System*

Following the system design and prototype creation, optimal/acceptable output parameters should be obtained and therefore tested. As such, not only will those outputs be evaluated directly, but the input parameters (of which some are outputs of a different system) should also be ensured to be operating as desired. To achieve this, the following tests are considered below.

### Magnetic Flux Generation

To ensure current is used ideally to create the magnetic field, an ammeter can be connected at the beginning and end of the coil wiring. It should be equal at input and output, otherwise may be indicative of leakage/unideal behavior. The magnetic flux in both the iron cores moving through the coils (circumferential) as well as towards the central arena (radial) may also be measured directly using a fluxmeter. Since different coils will be used simultaneously to control the  $\mu$ -bots, the positional deviation of the bots from the desired position will be used to establish the error bounds of the flux at the tips of the cores. The flux at the circumferential cores should not surpass half of the saturation flux density of the material, as this would lead to wasted current and more heating (flux at radial cores is the sum of its 2 inputs).

### Maintenance of Operational Temperature

The coils should not exceed a certain operational temperature in order not to affect other sensitive components of the controller. The critical temperatures to consider are the boiling point of the coolant, melting point of the wire insulators, and Curie point of the circumferential cores. To avoid coolant evaporation, should the temperature of the system be increased, flow rate/coolant pressure at the inlets can be increased. This will lead to more cooling, as well as increased boiling point of the coolant. Thermal sensors at the outlets may be used to monitor coil heat dissipation.

To continue, the wires should never reach a temperature near the melting point of their insulator (most insulators melt around 260-290 °C). Should this happen, sections of the coil may fail, and operation of the device may be unsafe. From the simulations, another thermal sensor should be attached to the hottest reachable region in the coil.

Finally, the cores through the coils should not be heated past the Curie temperature of iron, which causes irreversible damage past 730°C, and so is not of concern due to the other restrictions. However, core magnetization decreases with temperature (reversibly), and so higher working temperatures limit optimal performance, and should be minimized. To address this, coolant may be allowed to flow between the core and the inner interface of the coil.

#### *Microrobot Design Testing*

We want to see whether a response can be seen in a manganese solution. There are two methods of testing. We can test using prototypes of the solenoids that we create, which would serve two purposes of both validating results of solenoids testing and testing the microrobots. An alternative to that testing method is contact Prof. Veronika Magdanz in Systems Design Department. Her lab has a solenoid setup system that is like what we are trying to build. If she provides us permission to use the setup in her lab, we can verify the design by exposing the microrobots to magnetic fields like what we plan to expose them to in our system.

The testing of the movement of microrobots is similar to the testing of the control system UX/UI. However, the testing of microrobots is there to verify the fabrication process of the robots and also to determine hydrodynamic properties.

A passing result would be one in which the movement in microrobots is visible in manganese solution and one where the materials used have been previously reported to be biocompatible. Scripts have been developed to track the movement and orientation of the anisotropic particles. The verification of the microrobots would include the robots behaving within certain tolerances. We would not want the microrobots to for example turn 20 degrees when the desired rotation is - 80 degrees. The tracking software would be able to track the orientation of the microrobot up to 180 degrees. This can be used to track the rotational tolerance of the microrobot. A passing error would be of 30% (with a high error rate being present due to fabrication error that is inherently present in this iteration of design).

This is coupled with translational tolerance. Python scripts have also been created to track translation in the x-y cartesian plane. A similar requirement is placed on movement in the x-y cartesian plane. We would not want the microrobots to move to (x,y) location (-1,2) when the desired end location was (3,1). Similar error rate is going to be placed on translational component. A passing test would be one where the error of the translation is 30% (the error rate being high for the reason of inherent error in fabrication at scale).

Furthermore, a passing result would mean the actuator are either millimeter scale or micrometer scale. The fabrication of the microrobot should not result in a high variability in sizes of the microrobots. Part of the verification of this aspect of the microrobot can be encompassed by the previous test of translation and rotation.

Lastly, the hydrodynamic scalar coefficient needs to be tested. This value can be tested for by assuming that particle has a spherical hydrodynamic radius. The particle's Brownian behaviour can be tracked in a fluid using python scripts and ImageJ software. This information can then be

used to determine the diffusion coefficient of the particle. A successful test would be one where the experimental diffusion coefficient has the same order as the modelled diffusion coefficient. The hydrodynamic radius can then be calculated from this value using the same relations mentioned in the verification section.

## Appendix D

### Preliminary Design Specifications

#### *Hardware / Software System*

Figure 5 shows the hardware that was used for the whole low-level system. As this device is essentially a magnetic power delivery system, most of the electrical hardware is centred around power distribution. 120V mains AC is fed from a switched male outlet into an adjustable 24V, ~20A power supply. The adjustment potentiometer is present on the control panel, alongside an indicator light for DC power in the system, and a resistor has been soldered to both output terminals to restrict the output voltage range from 6-24V to 10-20V. This is done to match the stable voltage input range of the Pololu motor drivers. On top of DC voltage input, each channel of the motor drivers' logical input and current sense output feeds to the control module. A switch was added to interrupt the live 120 V AC when the device was desired to be off but not unplugged. The 24 V from the power supply is then connected to all three Pololu motor drivers as the power input as the power supply supplies the power used to drive the magnetic coils. To power the Teensy 4.1, The 7.5V power output from one of the Pololu shields was fed through a 5V LDO regulator. Output from the drivers to each coil is routed along the top inner edge of the enclosure.

Proceeding with the data connections between devices, a USB port is installed on the frame of the device which was connected to the Teensy 4.1. This allows for interfacing with the Teensy 4.1 for convenient programming and external communication. For the connection between the Teensy 4.1 and the Pololu motor drivers, PWM is used to control current magnitude, and a binary signal controls direction. Two other connections exist per motor driver which includes current sense, fault sense. These connections allow the controller to continuously monitor each coil throughout operation. This concludes the low-level hardware for our system.

For our low-level system, this consists of two components being software run on our host computer, and the software running on the Teensy 4.1. The software that is run on the host computer consists of the Python code that takes in controller inputs and maps them to control vectors that are inputted into the Teensy 4.1. This code consists of first pairing with the Bluetooth XBOX controller. Once a connection is established, the inputs are mapped, and the raw values are obtained and converted to a scale of values with a max magnitude of one. These values are then mapped to control vectors through the code we used in our simulations with some adjustment factors. Once the control vectors are generated, they are sent over USB to the Teensy 4.1.

For the code running on the Teensy 4.1, this consists of taking our control vectors from the computer and sending the commands to the motor drivers. The code first starts by opening a communication port, to which it receives the control vectors from. The control vectors consist of six numbers, each number representing one coil power magnitude. When the Teensy 4.1 receives a control vector, the new position is sent to the motor drivers to change the current through each coil. To interface the Teensy 4.1 and the motor drivers, Pololu has source code for a library. The issue with the library is that it only supports the use of one board. As we use three, the library was modified to support the use of three boards and 6 coils simultaneously. This allows us to address each of the six coils. The cycle of receiving and setting coil currents then repeats.

### *Mounting system*

Our finished prototype contains three major subsystems: logic electronics, power electronics, and heat management. Each of these three systems must be isolated from one another. Our mounting system has been designed to achieve this isolation while being as compact as reasonably possible and showcasing the magnet array on the top surface of the prototype. The cosmetic/display aspect

of the prototype was a resounding success, and it's form likely distracted from the gap between specified & demonstrated performance.

The logic electronics must be shielded from the power electronics and magnet array, and all electronics need to be suitably protected from the water flowing through the coolant system. Shielding will be provided by mounting our logic electronics within a simple Faraday cage. This was envisioned as being constructed of sheet steel but was implemented using aluminium HVAC tape for spacing & manufacture time. No leak protection was implemented, as this feature only served redundancy, and making the upper tray watertight didn't seem worth the time and effort.

Winding of the coils will be performed using a home-built and tested magnet winding system, that is powered by a cordless drill, tensioned by an adjustable brake on feeding spool, and stabilised by a pulley on a spring. Coils were initially specified as containing 1Lb of 26AWG wire, but construction used 28AWG wire and were quantified by number of turns instead of mass. This shift drastically reduced coil cost, allowing excess wire to be supplied in case of coil failure.

#### *Magnetic system*

- 1- The horizontal bandsaw was first used to cut the steel blanks to rough length and angle. 8 blanks (2 extra) were cut for both geometries (3.5" parallelogram and 4" rectangle).
- 2- Following this, the milling machine was utilized to ensure the four sides of each bar were perfectly parallel to one another. This step was crucial for maintaining consistency and alignment once the bars were mounted.

3- Finally, the belt sander was used to shave off sides of the bars relative to a reference bar to ensure all bars had a uniform thickness. Both this step and step 3 ensure the flux across all 6 bars is uniform.

To focus and redirect the magnetic fields that our system produces, we need a structure of material that can conduct the magnetic fields, can be easily shaped, and is reasonably priced for an initial prototype. On top of this, we would like our magnetic system to exhibit the lowest feasible hysteresis. To achieve this, we plan on machining the lens components from hot-rolled steel due to its high average magnetic performance. A high-temperature annealing step was planned to improve consistency in the lens components, but access to a lab oven wasn't secured. A homemade forge using a propane torch, and sugar/pearlite-insulated coffee can was considered, but not attempted due to the impossibility of temperature control in such a system.

Forming the steel components of the lens was challenging due to the physical hardness of the material and required precision of the fit. Any gaps between lens components increases the magnetic circuit's reluctance significantly and lowers its efficiency and accuracy. Ultimately, A scaled model of the simulated geometry was constructed to meet the required precision, with each part only requiring 3 operations:

- Cut blanks to rough length and angle ( $\pm 1/8"$ ,  $\pm 1^\circ$ ) on bandsaw.
  - Both vertical and horizontal bandsaws were tried for this step, and both machines proved efficient and effective.
  - Horizontal bandsaw offered much more precision at better convenience with its calibrated protractor/ruler, hydraulic feed, and built-in vice.

- Square faces to rectangular profile ( $\pm 0.020"$ ) on vertical mill.
  - Rolled steel has 2 near-parallel faces from alignment of the final 2 rollers of the extrusion chain, while the other 2 faces bulge out.
  - Precise mounting of the lens components is much easier if all faces are square and perpendicular, & this operation can (in theory) be carried out easily on a mill.
  - We really don't know how to use a mill, and this operation turned out quite poorly, with a slope of about 12 thou across the parts' length and a choppy surface finish.
  - We likely should have properly trammed the mill & used a fly cutter, but our inexperience makes informed decisions difficult.
  - Fortunately, this doesn't impact performance too much. This face doesn't mate with lens components, and all materials that it contacts are poor magnetic conductors. Thus, magnetic coupling in these faces is weak, and relatively little of the total conducted field interacts with any of these scars.
- Bring mating faces to final grind ( $< 0.005"$  misalignment) using a disk sander.
  - Unmodified face was referenced to the fence, which was set to  $60^\circ$  using a machinist's protractor. High pressure on the fence was maintained for consistent alignment for both grinds.
  - Grinding was done slowly & with light pressure for precise grinding, and to protect the material from overheating, which would unpredictably change its magnetic properties.

- The Fence was swept from the disk's center to edge, allowing local inconsistencies in the sanding disk to be averaged out, leaving a surprisingly flat, even surface. This process was done on each end of each part in one session, ensuring consistent flatness and angle across all grinds.
- Consistency of parts' lengths was verified by designating the first finished part as a reference and placing each subsequent part beside it on a flat surface. The endpoint of each grind occurred when an edge couldn't be felt between the finished part and the reference on both ends simultaneously. As human touch can register features on the order of microns. Swapping the positions of each part and repeating the test verified that each part's profile was consistent.
- Accuracy of the angles was verified by clamping all mating faces of 5 of the trapezoids together and testing the final one's fit. For this test, a small gap in the final fit was preferred, as this ensures that surfaces touch on an obtuse angle (where there is more steel) than an acute one, minimising the impact of any imprecision.
- This entire process was repeated 3 times with slight corrections to the fence angle until a gap of  $1/64"$  was measured with a feeler gauge. As these were small corrections, and the parts were already ground to length, the correction process was much quicker than the initial grind.

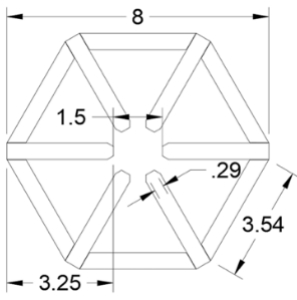


*Figure D.1: Dimensions of Magnetic System*

As the iron components are ground to a high precision, they can be forced into close alignment by applying pressure to the faces. This can be achieved by constraining the lens in the z-axis and providing even, radial compression. Mounting demands were met by embedding each mating lens face into a cut block of HDPE. Each block contains an undersized recess for both steel components it holds and staggered relief cuts along its height. This allows a shim to be placed in the back relief to clamp the joint in the z-direction, and clamping pressure can be tuned by sanding the shim, or adding masking tape. Each block also has a shallow hole drilled into its back side, which registers with a screw that protrudes in through the outer pine box. Clamping force from each screw is transferred to the steel lens through a block of plastic which is much softer than the steel lens. With the pressure delivered by twelve fine-pitch screws, the steel surfaces are forced into alignment while the plastic deforms. Coils were wound on a custom winding jig that consisted of 3 parts clamped to the top of a coffee table.

A feed spool of wire is placed vertically on a dowel, with its bottom face glued to a Styrofoam puck. This puck is suspended above another piece of Styrofoam through a layer of Vaseline which forms a planar grease bearing. Viscosity in the fluid bearing can be lowered by adding a few drops of baby oil, lowering the resistance of the spool to turning.

The wire is pulled from the feed spool through a pulley mounted on a spring. This exists to absorb any tension ripple from either temporary sticking in the grease bearing or the solenoid's elliptical profile, stabilising the tension in the wire for a more even wind.

Solenoid spools are placed onto split dowel which can expand by means of two screws to lock the core's position on the shaft. This shaft is mounted in a wooden frame via ball bearings and coupled to a driveshaft through a latex tube spacer. Winding is driven by a cordless drill at low speed, and alignment of the wind is performed by hand. Opposite to the drive shaft, winding is quantified using a cam to close a switch once per rotation. Pulses are filtered, debounced, and counted with a microcontroller which feeds to a laptop for easy display. This method of quantification was chosen over coil mass or resistance, as the number of turns most directly correlates to magnetic output. This choice introduced some inconsistency into coil resistance, the consequences of which are discussed in appendix F.

### Passive Cooling

The thermal conductivity of the windings is characterized by the 3 materials it contains (copper wire, the thermoplastic encapsulating it, and the air between the wires). As the air is the least conductive material, it is the constraining factor in passive heat flowing out of the system at the exterior interface. However, if the thermal simulations require it, the air can be replaced with a more conductive material, i.e. transformer oil. To do this, we can encapsulate the windings and core in an aluminum pipe, close off the edges, and fill the pipe with the transformer oil through 2 holes serving as inlet and outlet (outlet ensures this is filled). This system enables better passive cooling at the system's outer interface.

## *Actuation system*

### Actuator Prototype Construction

Table E.1: Ideal and Actual Components of Actuators

Raw material/part	Dimensions/Specs/properties
Aluminum Salt for Electroplating	Base layer that can be etched away using HCl [E.1]
Chromium Salt for Electroplating	Electroplatable metal that has magnetic susceptibility of 3.5e-6 [E.2] Minimum Radius and length of 100um
SU-8 Photo Mask	Photo-crosslinked polymer with Magnetic permeability of 1.08 [E.3] Minimum Radius and length of 100um

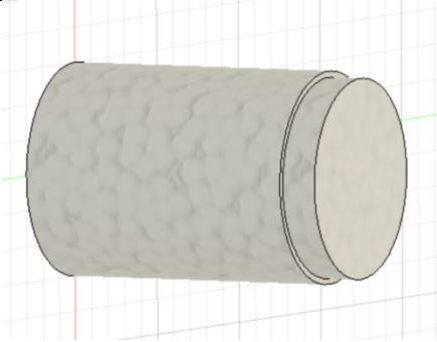


Figure D.3: Left section is Diamagnetic, Right section is Paramagnetic

The ideal actuators have five defined specs, namely radius, length of diamagnetic, length of paramagnetic, and magnetic susceptibility of both components. For the development of these specs, the actuators are modeled as point magnets with the infinitely thin bar attaching the two components as seen in Figure D.3. The fabrication procedure experimented in lab was designed to construct fabrication in Figure D.3, however, the final actuator deviated from the design significantly and can be seen in Figure 9: Oil Bead Actuators. This section will explore both the failed fabrication process, and fabrication process for the final system.

### Actuator Fabrication Process

The choice of paramagnetic material was difficult due to the limited options in terms of material available. Furthermore, another limitation for the design was the salt used for the Magneto-Archimedes solution. The plan is to use Fe[II] based salts, and the Pourbaix phase graphs for Iron force use to pick a material that is present in metal form at the pH and redox potential of the solution. Nickle and Cobalt both exist in the

solution form as seen in Figure D.4. Chromium on the other hand is in the metal phase which is why we selected the material.

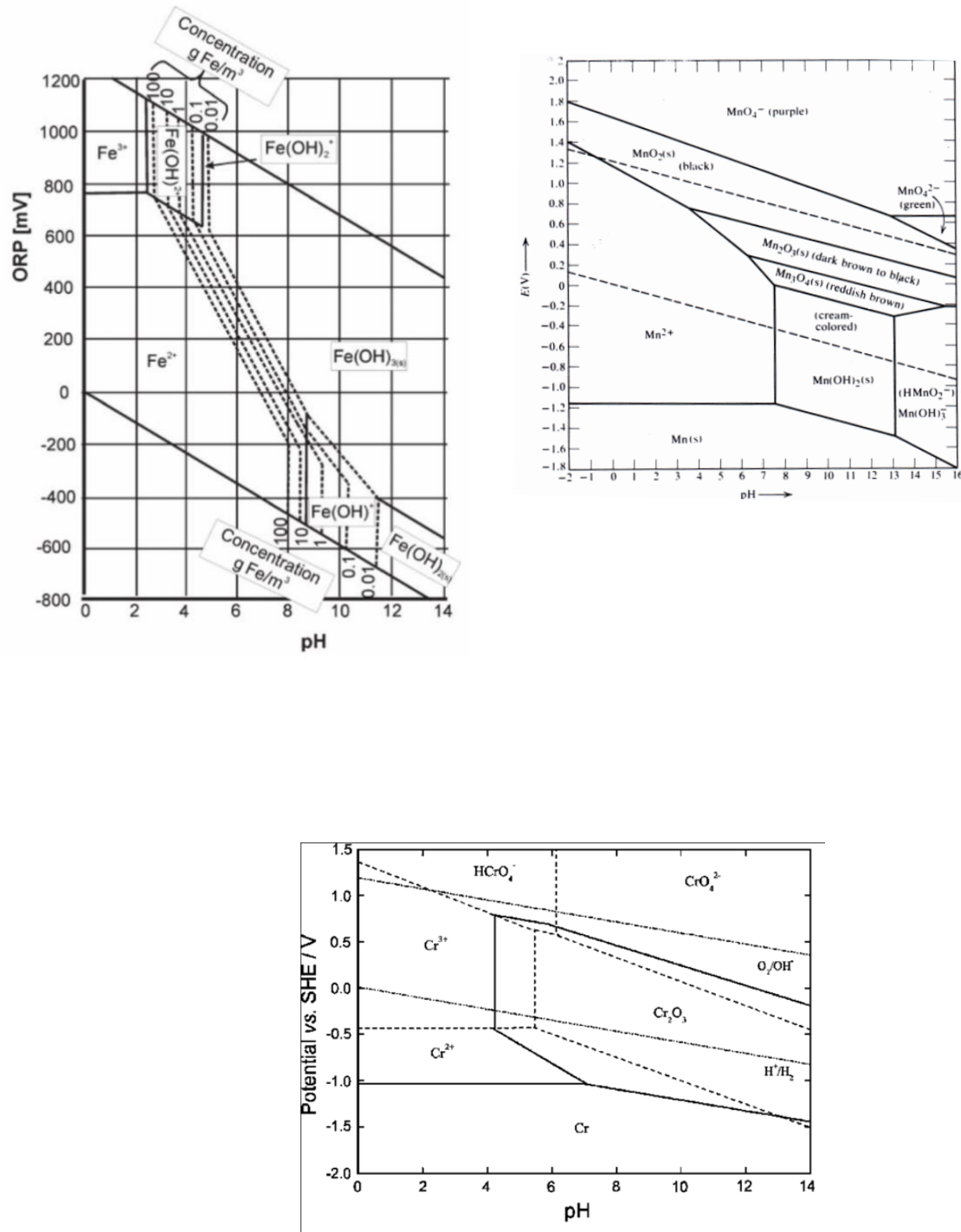
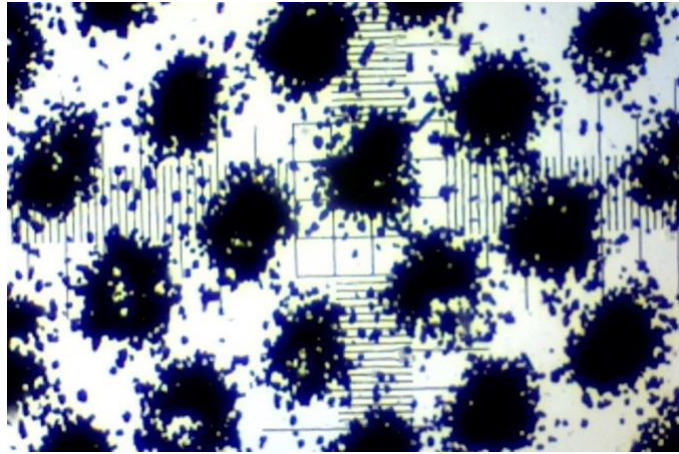


Figure D.4: Pourbaix diagrams [E.4] [E.5] [E.6]

For the diamagnetic material, SU8 was chosen due to the ease of deposition compared to Bismuth or polystyrene. SU8 is also resistant to acid [D.7] and allows for use of photomasks for the manipulation of the surface morphology. It can therefore act as a protective layer for paramagnetic component and has the right level of magnetic susceptibility. The length and the radius of the material are limited by the masks we can generate. The approximate range of the masks we can print with a laser printer can be seen in Figure E.5. It is a scale of about 100 m at the lower end, setting the minimum length and radius of the actuators to 100  $\mu\text{m}$  using this fabrication method.



*Figure D.5: Minimum Feature Size of Masks*

Fabrication procedure for the actuators designed can be found below. The sacrificial layer used is Brilliant Yellow, which is water-soluble. Initially, an Epoxy layer is spin coated and soft baked, and then another Epoxy layer is spin coated and filled with Aluminum. A mask is created using a laser printer and transferred via contact printing. Refer to Figure 6 below for a visual representation of this procedure. Soft bake procedures differ whether DLP resin or SU8 is used. SU8 2100 requires soft bake time of about 20 min at 230+  $\mu\text{m}$  thickness with spin coating speeds being about 1000 rpm [15]. Exposure dose at this thickness is about 370  $\text{mJ/cm}^2$  and development time is about 20 mins. DLP resin used was reppraper 202, with spin coating, soft baking, and development times

(in isopropyl alcohol) times not being available online. A range of values were tested with SU8 values being the starting points.

The 405 nm wavelength required for curing the DLP resin could be generated using a lab lamp. Despite attempts, the DLP resin was eventually deemed unsuitable as it led to the dissolution of the sacrificial layer. This is clearly illustrated in

Figure 7, where the DLP resin is seen to form droplets and erode the sacrificial layer.

SU8 2100, which was sourced from IDEATION lab, was used as the epoxy layer in the experiment. The manufacturer's website was referred to for the protocols but attempts to transfer the pattern onto SU8 were unsuccessful. As depicted in Figure 8, the developed SU8 showed cracks and a lack of pattern.

In the end, the actuator design had to utilize the oil-based method, which was briefly mentioned in the design verification section. This decision was primarily driven by the simplicity of the bead, which was made by mixing baby oil, iron, and bismuth filings. The beads were then placed between a layer of isopropyl alcohol and a solution of saturated iron (II) chloride. Figure 9 depicts the configuration of the system. Baby oil was used as the oil phase and bismuth and iron filings were produced using a sandpaper of various grit. The filings were thoroughly mixed in oil phase and until the mixture was uniformly distributed. Beads were created using a pipette or syringe without needle. The incorporation of the beads with solution can be found in the section below.

### Solution Chemistry

In Figure D.4, The Iron and Manganese Pourbaix diagrams can be seen. These graphs show that redox potential and pH the metals exist in the ion phase. The ion phase is important for the creation

of a paramagnetic solution that can be exploited for enhancement of the diamagnetic material. The strength actuator of the two components relative to the solution is modeled in equation E1 in Appendix E. The number of salts that work for the solution are limited, with Iron (II), Iron (III), and Manganese (II) salts being the best candidates for the solution. The Iron (III) atom is in the ion phase at a low pH and a high ORP. All salts were synthesized by us using commonly found reagents at hardware stores. Iron(II) Chloride is easier to synthesize than Manganese salts, eliminating Manganese from the paramagnetic phase all together.

The Solution has two distinct layers. The bottom layer is a paramagnetic solution consisting of Iron (II) Chloride and Sodium Chloride until saturation. The saturation is key as it prevents the organic layer from mixing. The organic layer consists of isopropyl alcohol, creating a 2D plane for insertion of beads/actuators. The Beads are created by mixing iron particles and bismuth particles in an oil phase. The particles are created using fine sandpaper. The oil solution can be dropped in drops in the solution and will settle in the 2D water/organic interface.

## References

- [D.1] N. Nnaji, . N. Nwaji, J. Mack and T. Nyokong, "Corrosion Resistance of Aluminum against Acid Activation: Impact of Benzothiazole-Substituted Gallium Phthalocyanine," *Molecules*, vol. 24, no. 1, 2019.
- [D.2] MIT, "PVD Chromium," [Online]. Available: <http://www.mit.edu/~6.777/matprops/chromium.htm>.
- [D.3] MIT, "SU-8 Photoresist," [Online]. Available: <http://www.mit.edu/~6.777/matprops/su-8.htm>.
- [D.4] Z. Ahmad, "CHAPTER 2 - BASIC CONCEPTS IN CORROSION," in *Principles of Corrosion Engineering and Corrosion Control*, ScienceDirect, 2006, pp. 9-56.
- [D.5] Western Oregon University, "Diagrams That Provide Useful Oxidation-Reduction Information," [Online]. Available: <https://people.wou.edu/~courtyna/ch462/redox.htm>.
- [D.6] G. Kear, H. Wu and S. M. Jones, "Corrosion of ferrous- and zinc-based materials in CCA, ACQ and CuAz timber preservative aqueous solutions," *Materials and Structure*, vol. 41, no. 8, pp. 1405-1417.
- [D.7] D. A. M, "Description of SU-8," 2005. [Online]. Available: <https://mesaplusnanolab.ewi.utwente.nl/mis/generalinfo/downloads/equipment/Delta%2020%20SU-8/Description%20of%20SU.pdf>.
- [D.8] ArduCam, "5MP Wide Angle USB Camera with Mini Metal Case, 1/4" CMOS OV5648 Mini UVC USB2.0 Video Webcam Without Microphone for Windows, Linux, Android, and Mac OS-Arducam," [Online]. Available: <https://www.arducam.com/product/arducam-ov5648-usb-camera-with-case-ub023301/>.
- [D.9] Amazon, "Xbox Wireless Controller – Robot White for Xbox Series X|S, Xbox One, and Windows 10 Devices - Robot White Controller Edition," [Online]. Available: <https://www.amazon.ca/Xbox-One-Core-Controller-Robot/dp/B08DF26MXW>.
- [D.10] Amazon, "Number-One Submersible Water Pump, 90GPH(350L/H, 4W) Water Fountain Pump Portable Water Pump Submersible Pump with 5.9ft Power Cord, 2 Nozzles for Fish Tank, Aquarium, Statuary, Hydroponics," [Online]. Available: [https://www.amazon.ca/Number-One-Submersible-Fountain-Portable-Hydroponics/dp/B07JP68SGX/ref=asc\\_df\\_B07JP68SGX/?tag=googleshopc0c-20&linkCode=df0&hvadid=292974432880&hvpos=&hvnetw=g&hvrand=18181193631690560646&hvpone=&hvptwo=&hvqmt=&hvdev=c&hvdvcmdl=&hvlo](https://www.amazon.ca/Number-One-Submersible-Fountain-Portable-Hydroponics/dp/B07JP68SGX/ref=asc_df_B07JP68SGX/?tag=googleshopc0c-20&linkCode=df0&hvadid=292974432880&hvpos=&hvnetw=g&hvrand=18181193631690560646&hvpone=&hvptwo=&hvqmt=&hvdev=c&hvdvcmdl=&hvlo).
- [D.11] G. Kear, H. Wu and M. Jones, "Corrosion of ferrous- and zinc-based materials in CCA, ACQ and CuAz timber preservative aqueous solutions," *Materials and Structures/Materiaux et Constructions*, vol. 41, pp. 1405-1417, 2007.
- [D.12] A. M. D, "Description of SU-8," [Online]. Available: <https://mesaplusnanolab.ewi.utwente.nl/mis/generalinfo/downloads/equipment/Delta%2020%20SU-8/Description%20of%20SU.pdf>. [Accessed 07 November 2022].

## Appendix E

### Verification Data

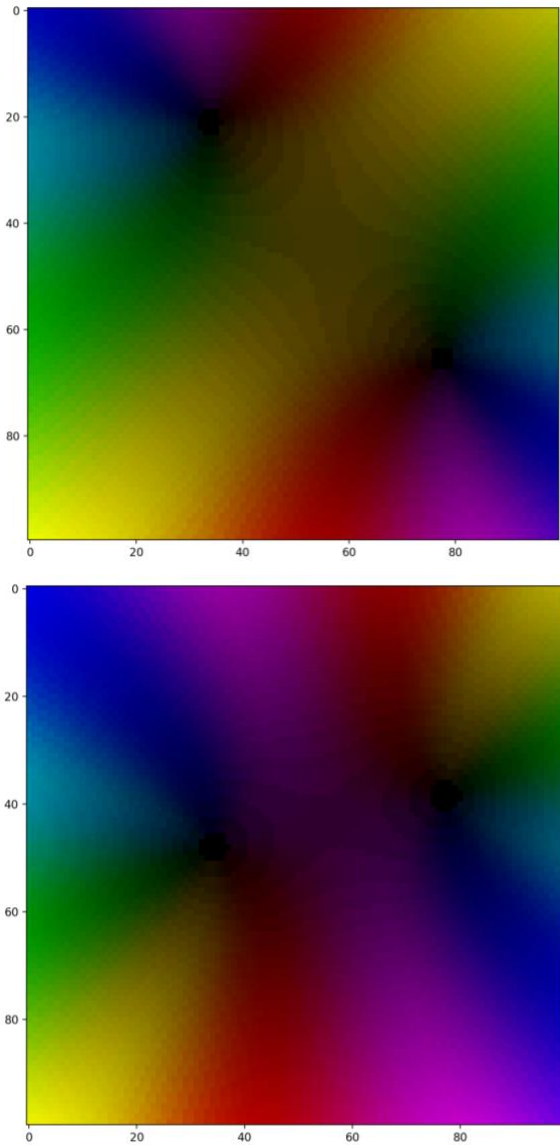


Figure E.1: Initial Prototype of Visualization Software Showing Actuator Potential (brightness) and Alignment Direction (hue)

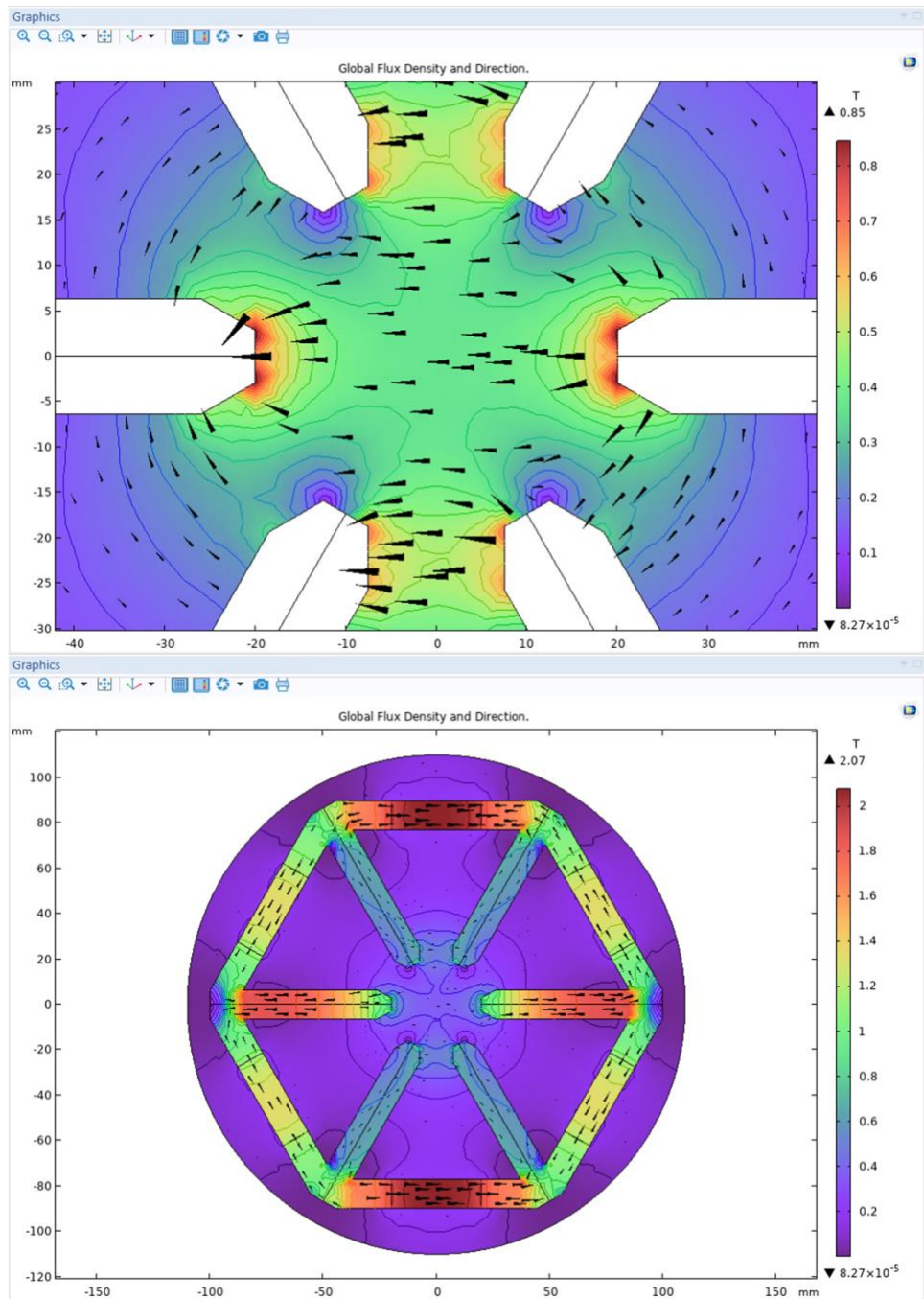


Figure E.2: Global Density and Direction for Normal Dipole

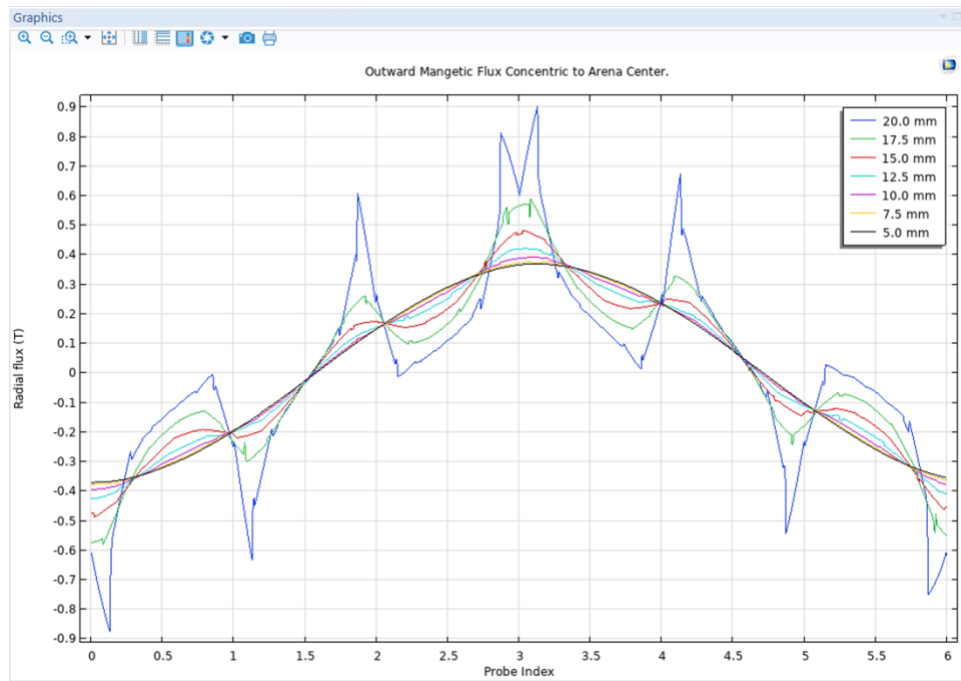


Figure E.3: Outward Magnetic Flux Concentric to Arena Center for Normal Dipole

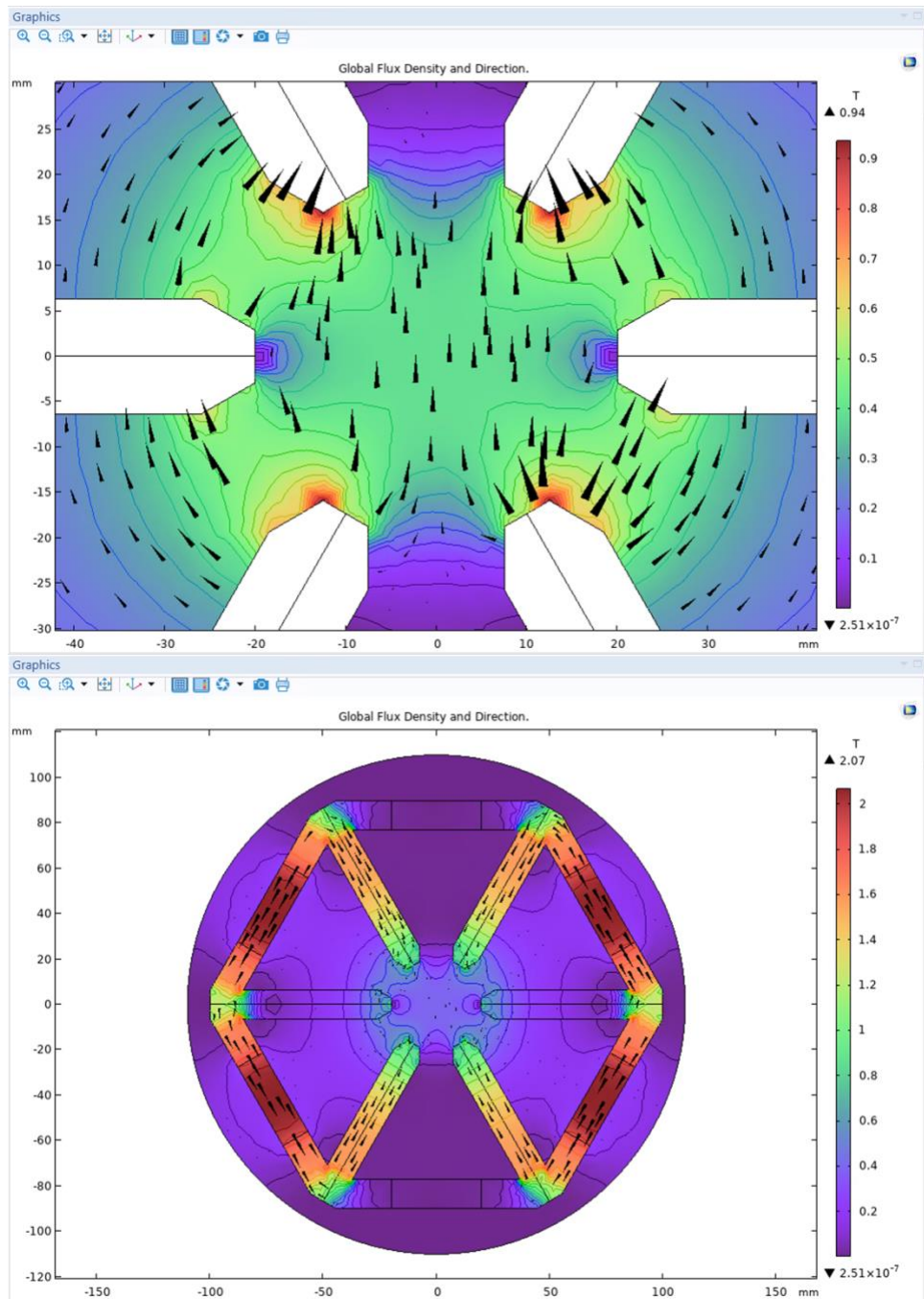


Figure E.4: Global Flux Density and Direction for Skew Dipole

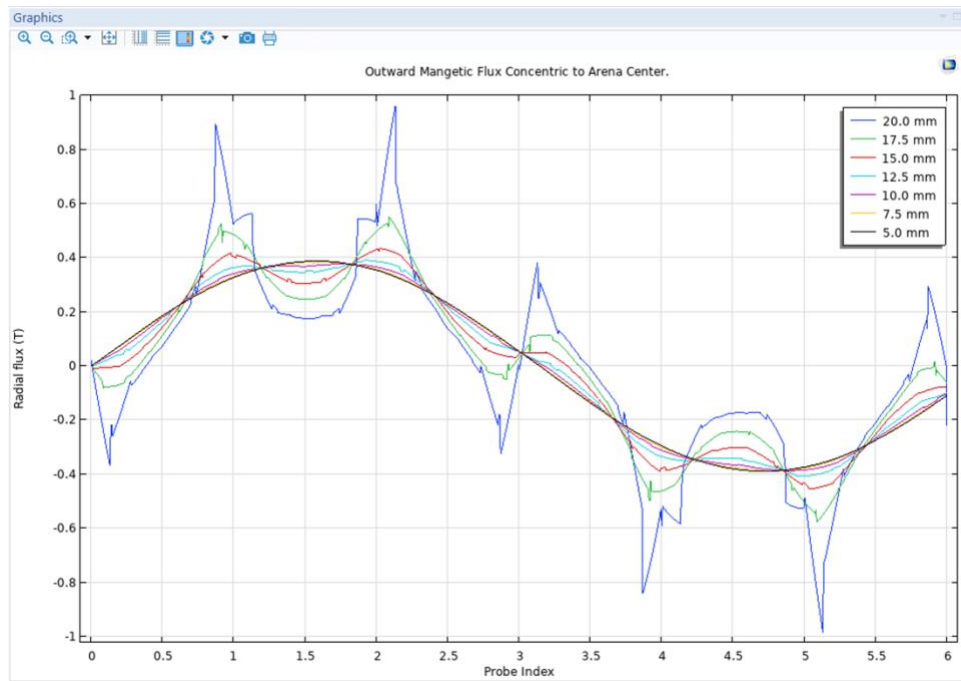


Figure E.5: Outward Magnetic Flux Concentric to Arena Center for Skew Dipole

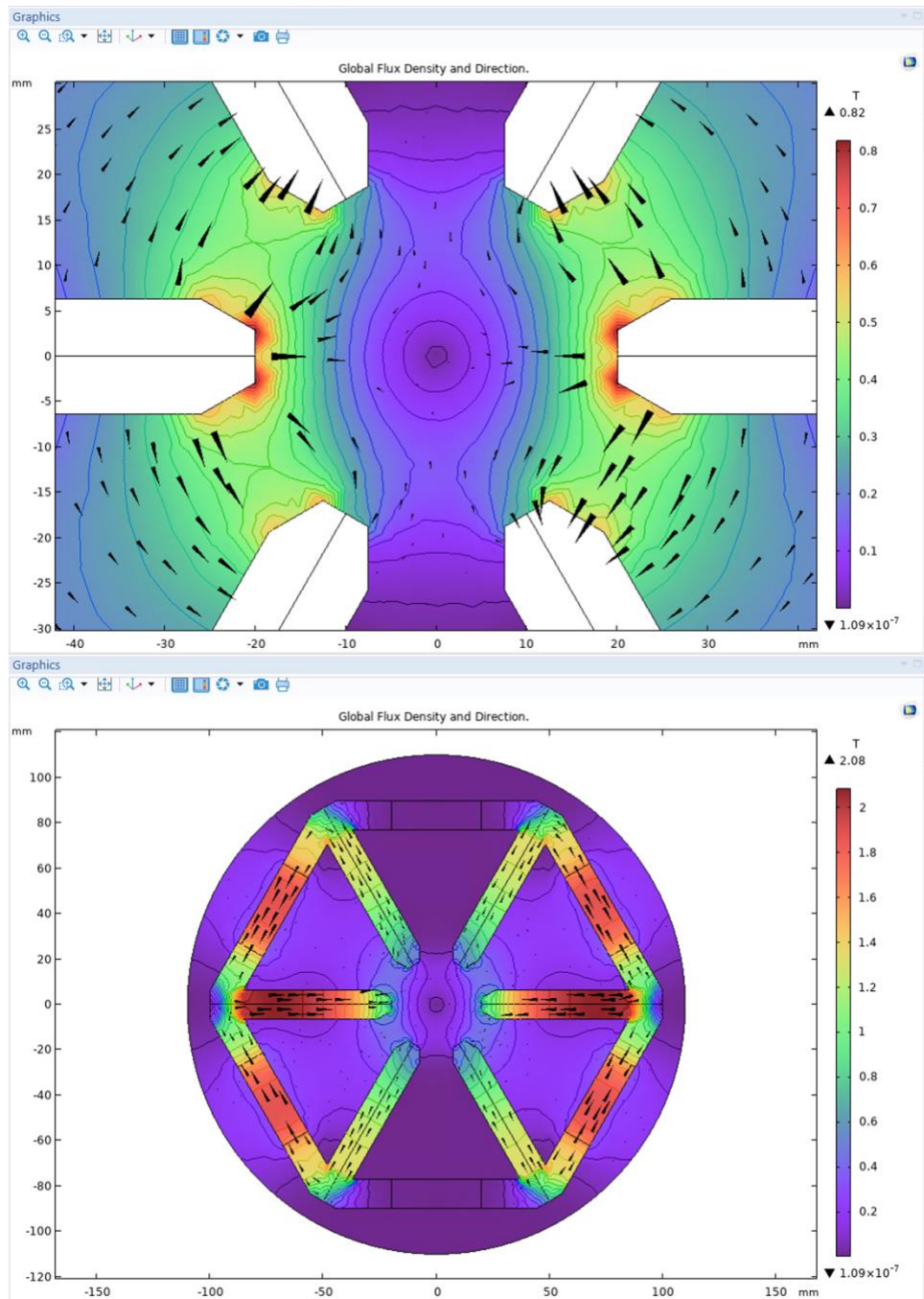


Figure E.6: Global Flux Density and Direction for Normal Quadrupole

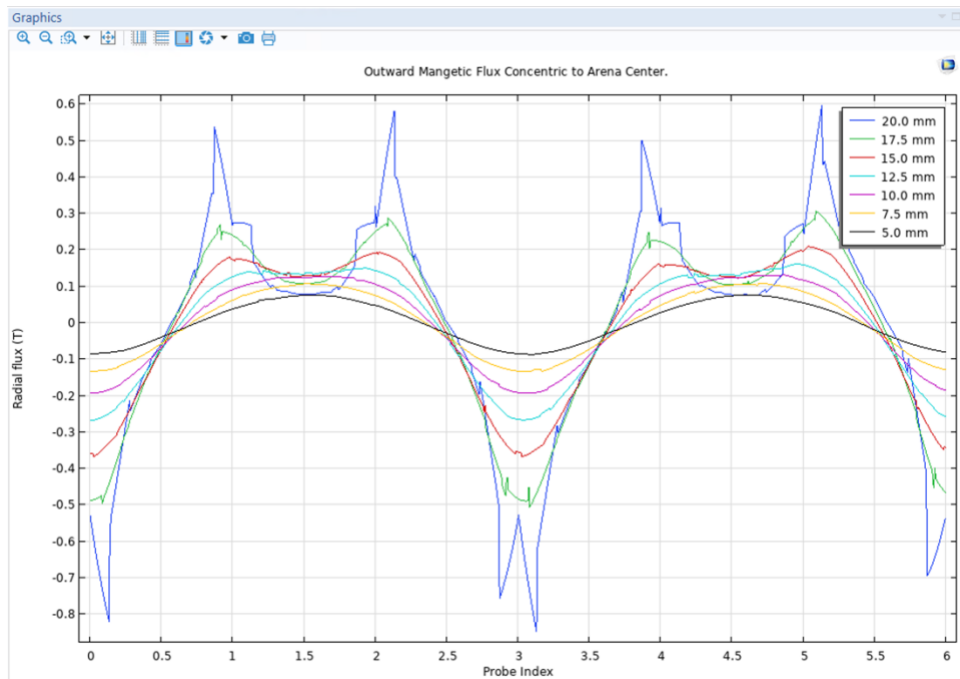


Figure E.7: Outward Magnetic Flux Concentric to Arena Center for Normal Quadrupole

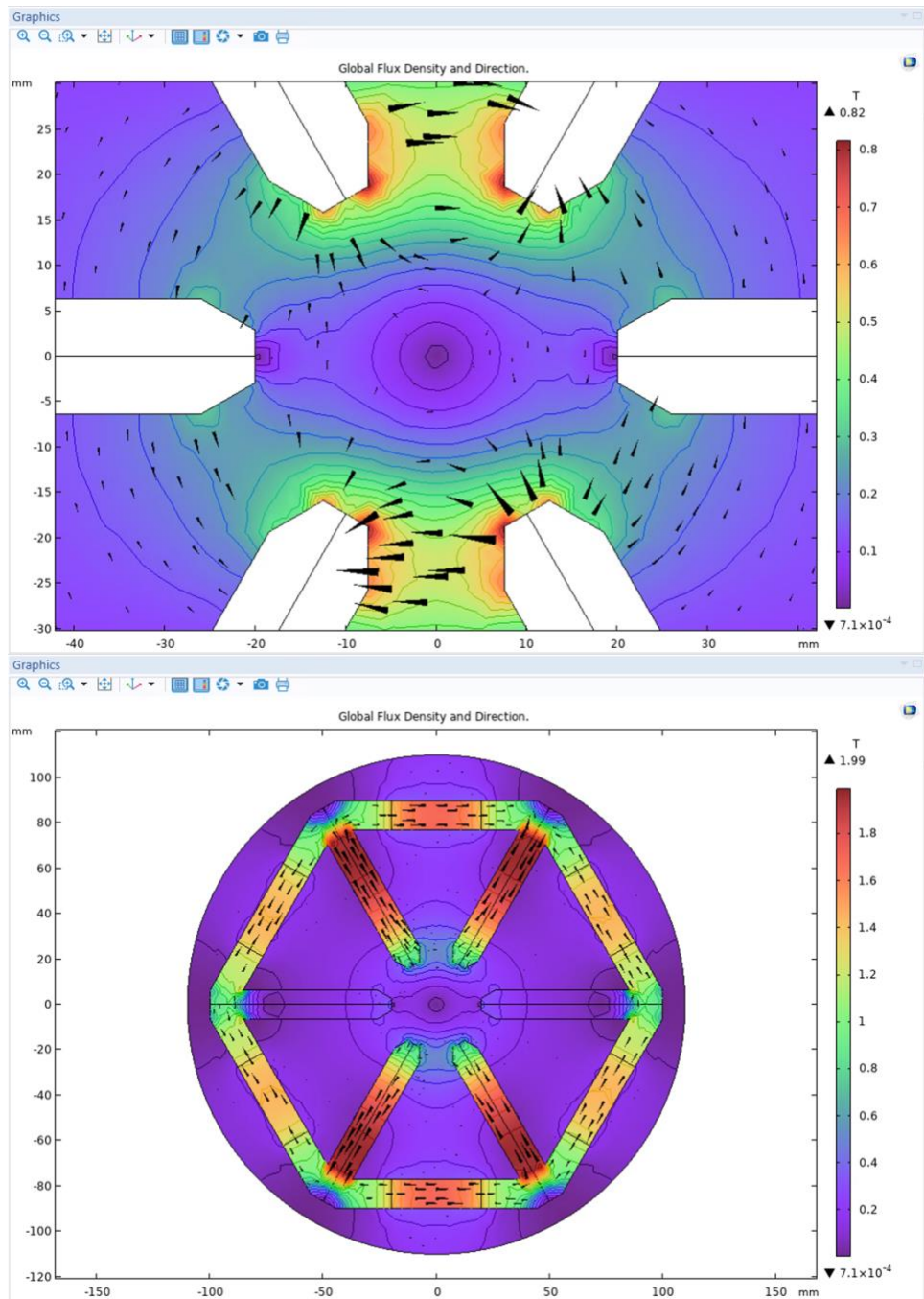


Figure E.8: Global Flux Density and Direction for Skew Quadrupole

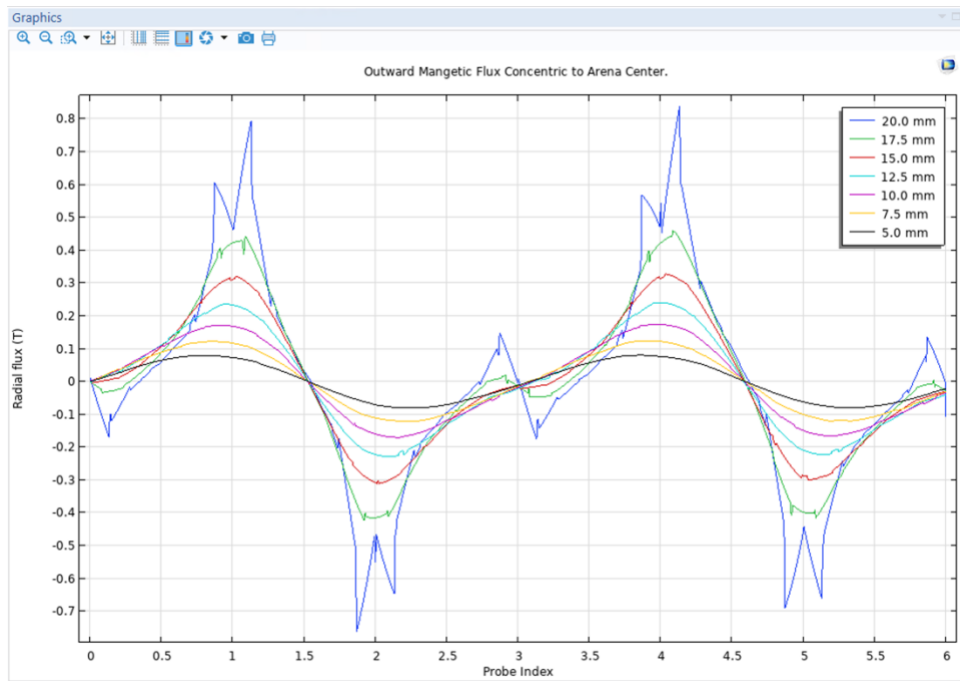


Figure E.9: Outward Magnetic Flux Concentric to Arena Center for Skew Quadrupole

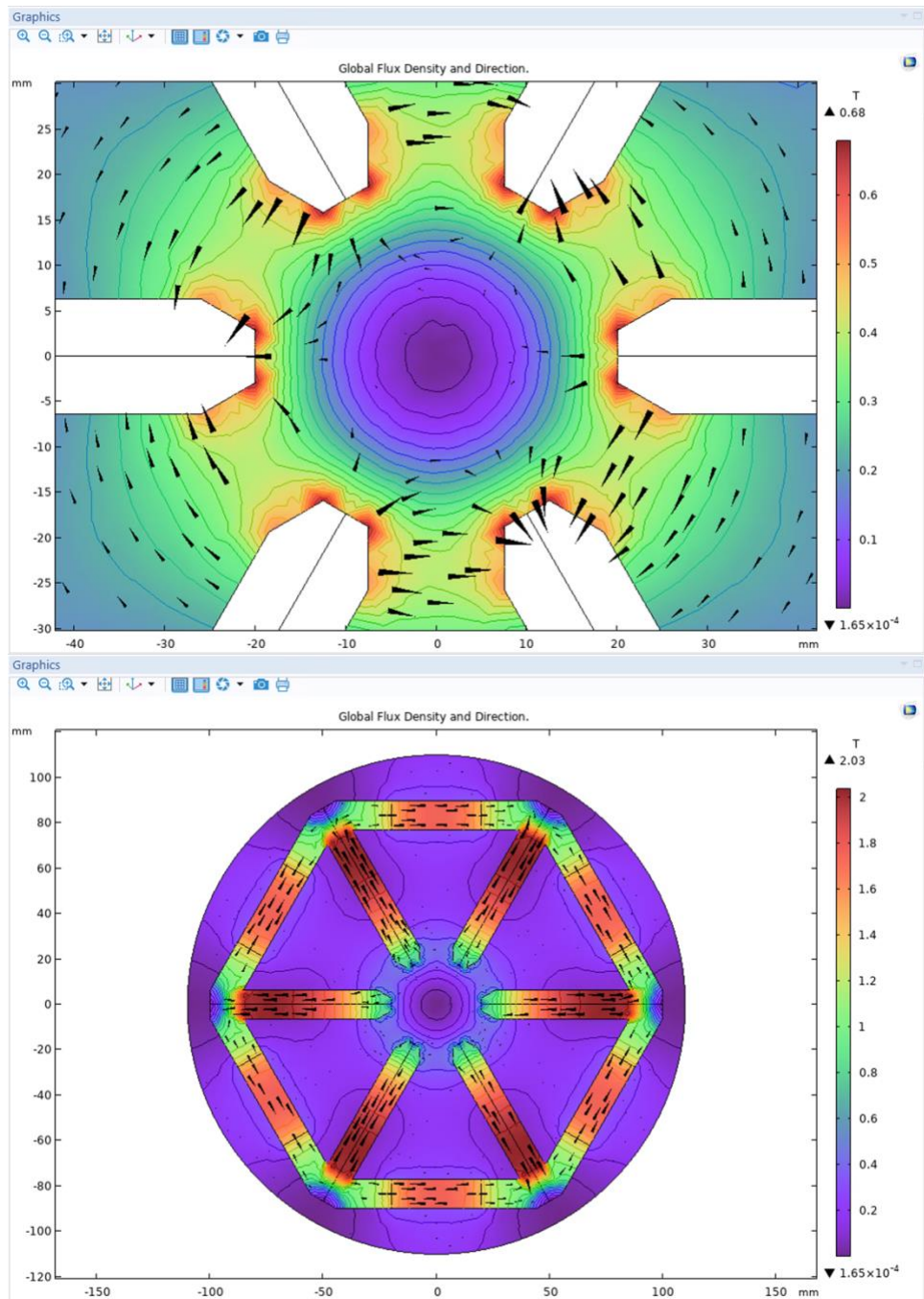


Figure E.10: Global Flux Density and Direction for Normal Hexapole

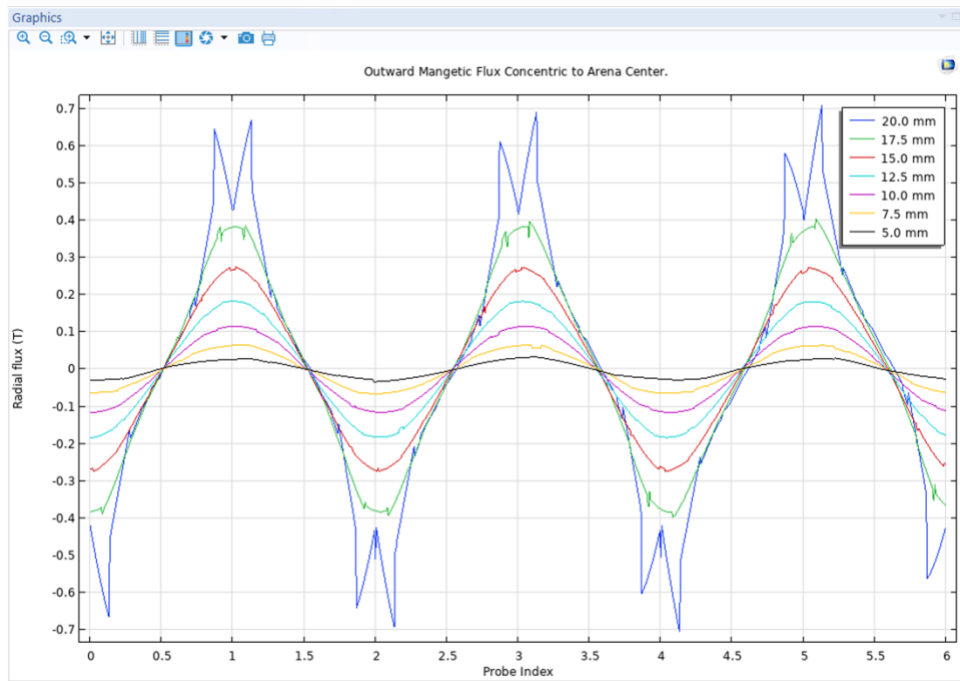


Figure E.11: Outward Magnetic Flux Concentric to Arena Center for Normal Hexapole

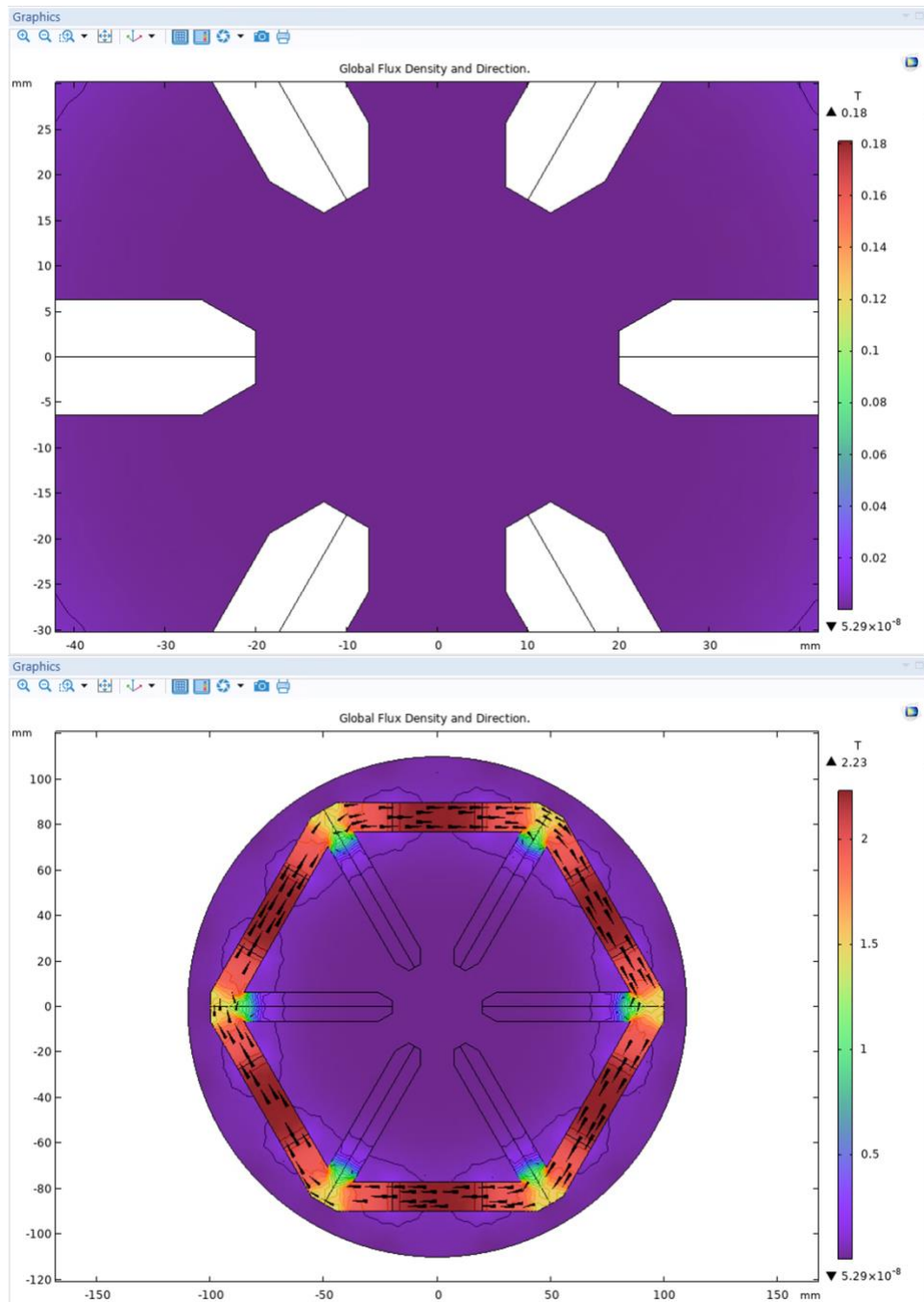


Figure E.12: Global Flux Density and Direction for Skewed Hexapole

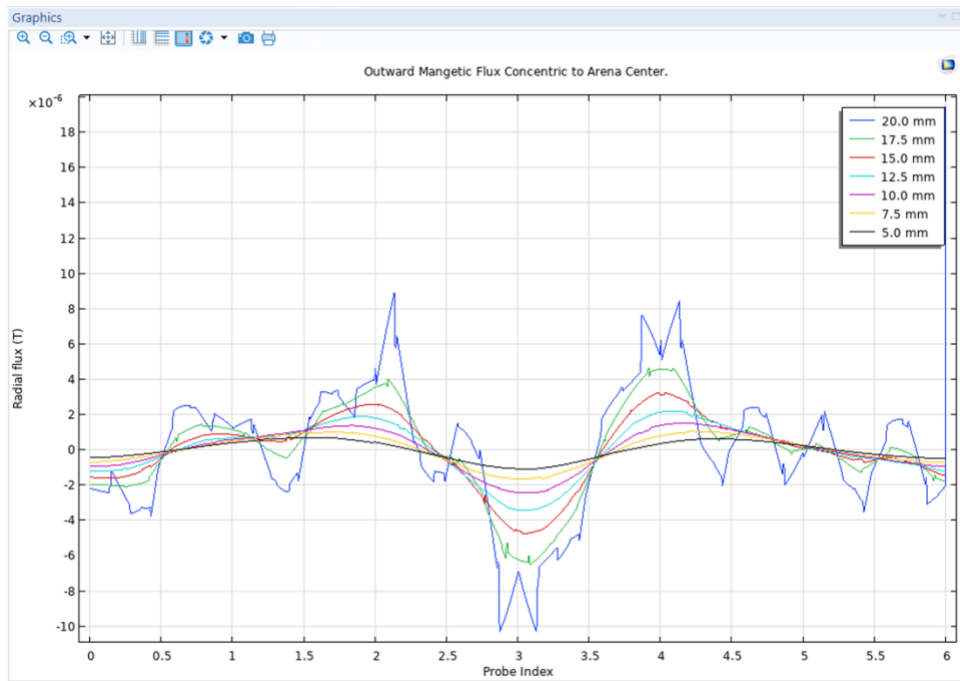


Figure E.13: Outward Magnetic Flux Concentric to Arena Center for Skewed Hexapole

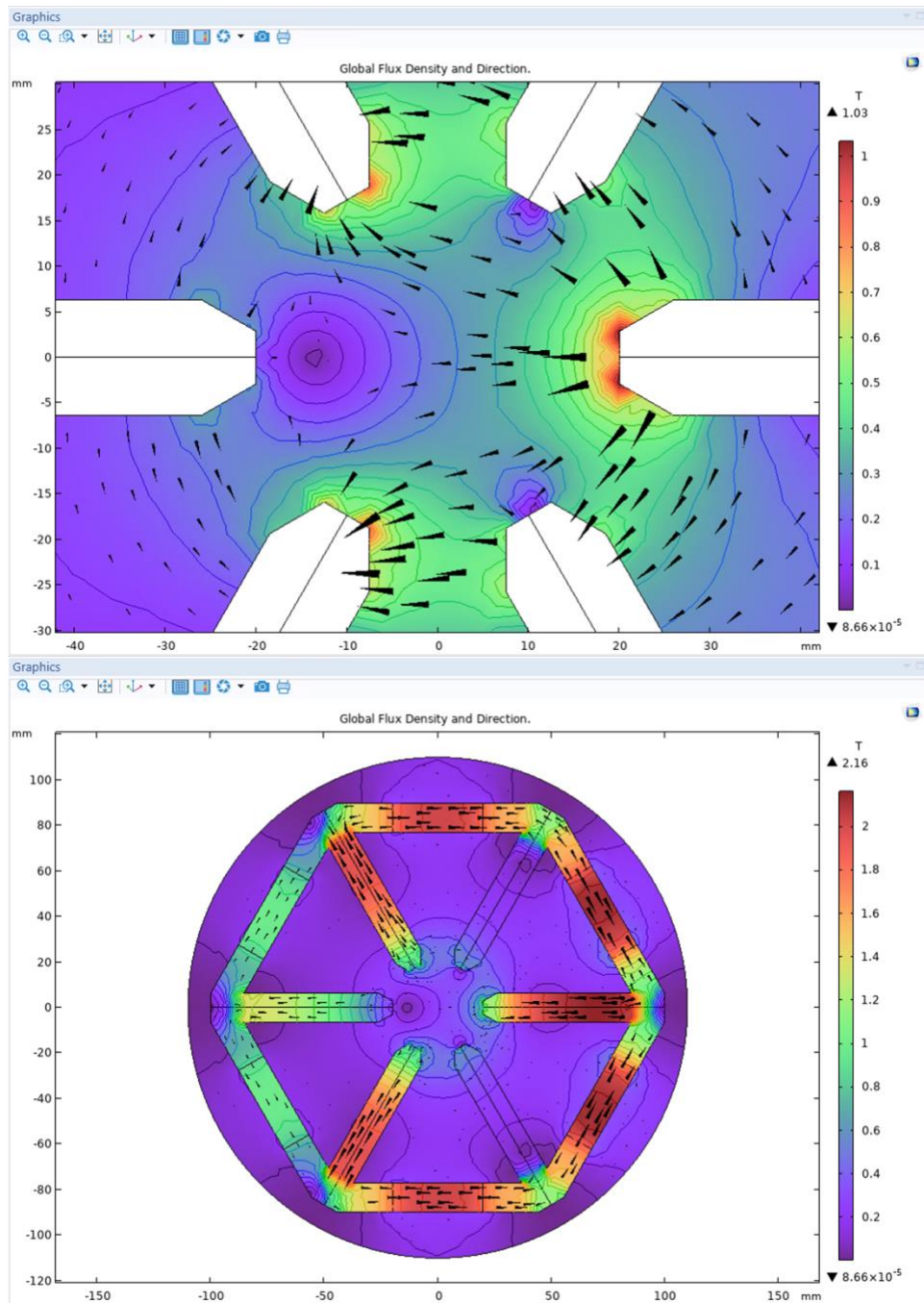


Figure E.14: Global Flux Density and Direction for Mixed Multipole, Example 1

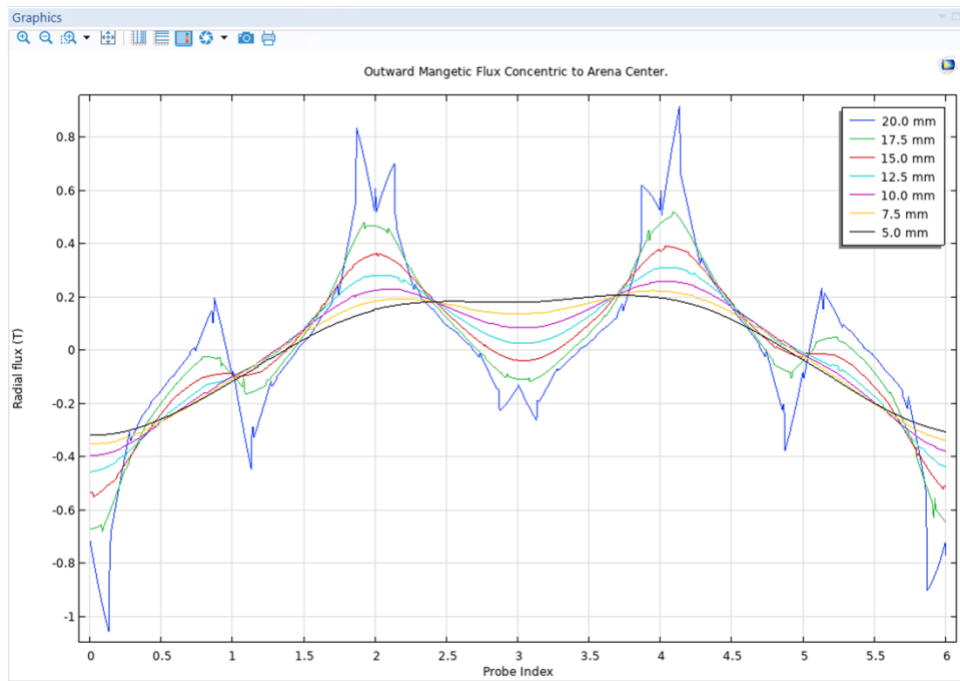


Figure E.15: Outward Magnetic Flux Concentric to Arena Center for Mixed Multipole, Example 1

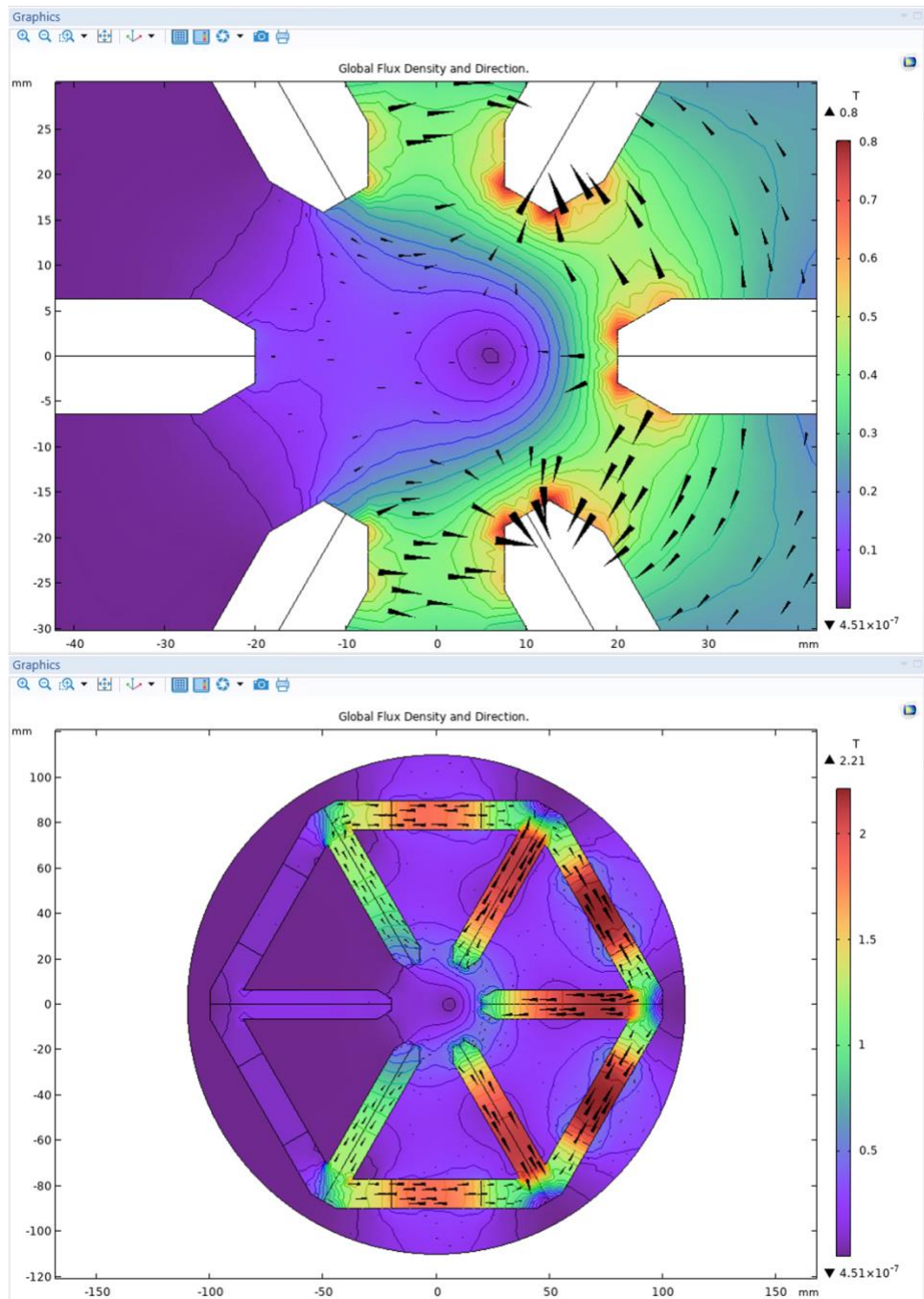


Figure E.16: Global Flux Density and Direction for Mixed Multipole, Example 2

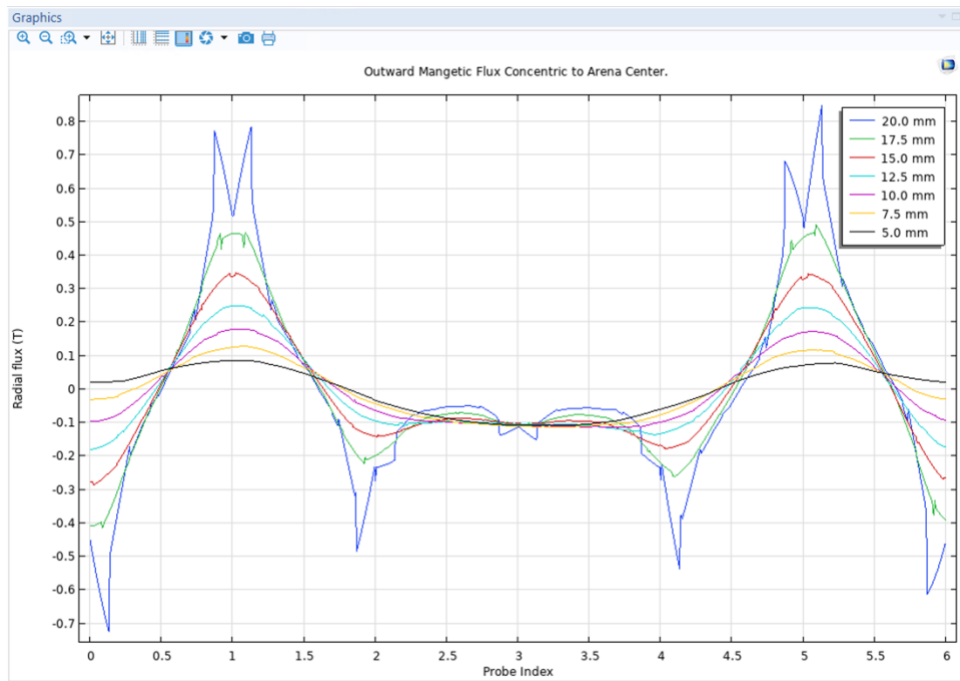


Figure E.17: Outward Magnetic Flux Concentric to Arena Center for Mixed Multipole, Example 2

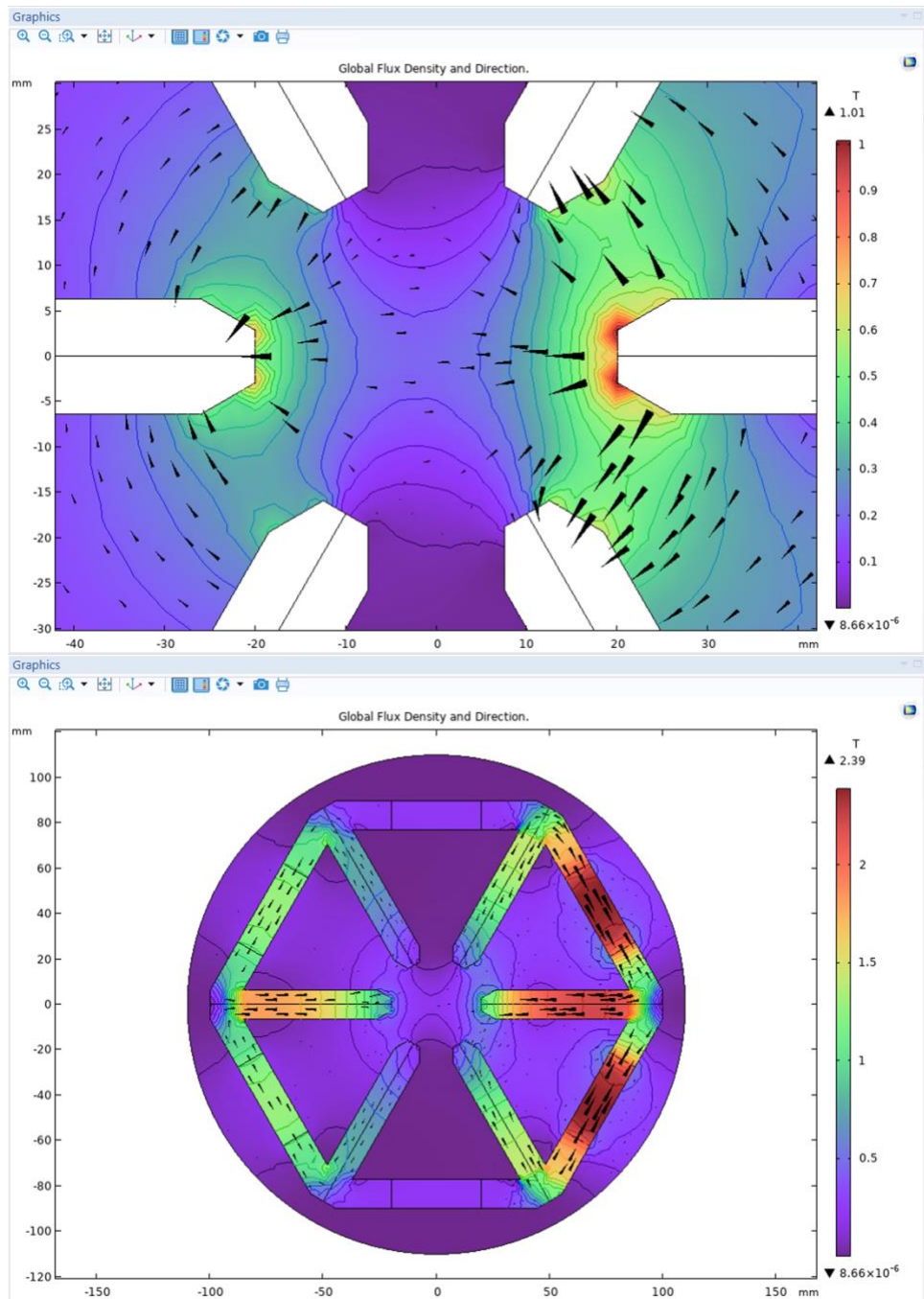


Figure E.18: Global Flux Density and Direction for Mixed Multipole, Example 3

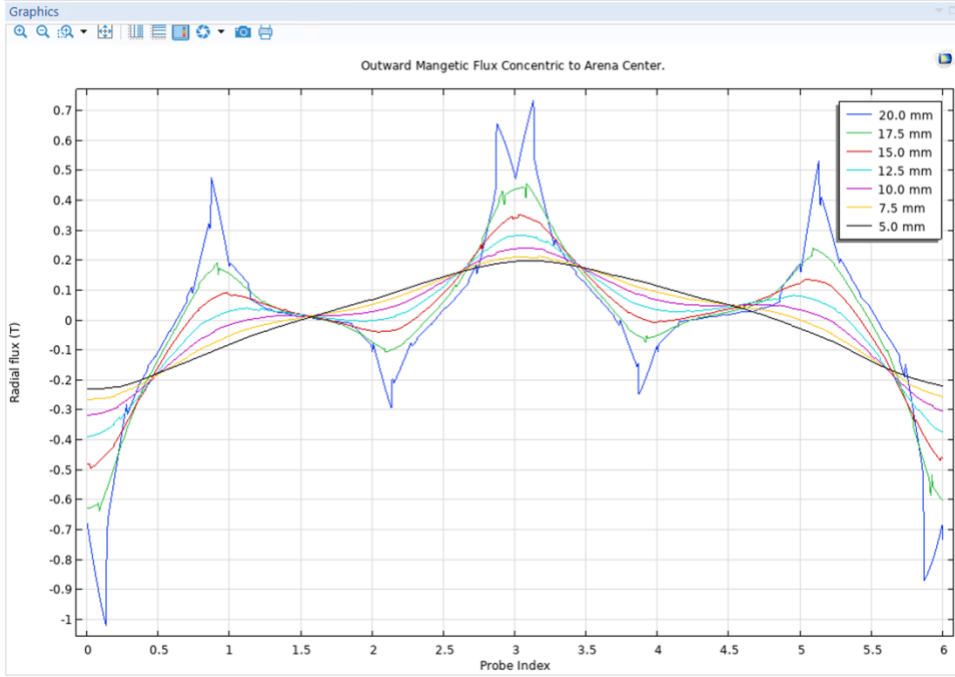


Figure E.19: Outward Magnetic Flux Concentric to Arena Center for Mixed Multipole, Example 3

$$\mathbf{F} = \nabla(\mathbf{m} \cdot \mathbf{B}) \text{ and } \boldsymbol{\tau} = \mathbf{m} \times \mathbf{B} = 0$$

Since  $\mathbf{B} = \mu \mathbf{H}$  and  $\mathbf{m} = \chi \mathbf{H}$ , We can say that  $\mathbf{m} = \frac{\chi}{\mu} \mathbf{B}$

$$\text{Giving us } \mathbf{F} = \frac{\chi}{\mu} \nabla(\mathbf{B} \cdot \mathbf{B}) = \mathbf{k} \nabla |\mathbf{B}|^2$$

Treating  $\mathbf{B}$  as complex unit with n poles leads to  $\mathbf{B} = \mathbf{R}^{(n-1)} \cdot \exp[(n-1)\pi i\theta] = \mathbf{R}$

$\mathbf{R}$  is to the power of  $(n-1)$  since we need at least 2 poles

$$\mathbf{F} = \mathbf{k} \nabla |\mathbf{B}|^2 = \mathbf{k} \nabla |\mathbf{R}|^{2(n-1)} = \mathbf{k}(2n-2)(\mathbf{R}^{(n-1)})$$

$$|\mathbf{F}_D| = |\mathbf{F}_P|$$

Lets say  $\mathbf{R}_D, \mathbf{l}$  is the center of mass of diamagnetic and length so

$$\mathbf{k}_D \nabla |\mathbf{R}|^{2(n-1)} = \mathbf{k}_P \nabla |\mathbf{R} + \mathbf{l}|^{2(n-1)} \text{ which leads to}$$

$$\mathbf{R} = \frac{\mathbf{l}}{\sqrt[n-1]{\frac{\mathbf{k}_D}{\mathbf{k}_P} - 1}} \text{ where } \mathbf{k}_D > \mathbf{k}_P \text{ for the system to be stable}$$

Equation E1: Stability Criteria For Actuators

$$t_{paramagnet} = \frac{400(-2\chi_{Bismuth})}{1.3(\chi_{paramagnet} - 2\chi_{Bismuth})} \mu m$$

*Equation E2: Actuator Paramagnetic Component Thickness*

## Appendix F

### Prototype Test/Measurement Data

*Table F.1: Prototype type/measurement data*

Customer Requirement	Test Results	Success Level
<i>Power Output</i>	Desired: 1 T <i>Actual: 0.8 T</i>	80%
<i>Locomotion</i>	Desired: x, y, $\theta$ <i>Actual: x, y, <math>\theta</math></i>	100%
<i>Control Mechanism</i>	Desired: Local control w/ PID loop <i>Actual: Local control</i>	75%
<i>Complex Local Control</i>	Desired: Local control w/ 5 DOF <i>Actual: Local control w/ 3 DOF</i>	75%
<i>Biocompatibility</i>	Desired: Literature backed bio compatible materials in actuator <i>Actual: Oil and metal based actuator not found to be safe inside body [12]</i>	0%

### Magnetic Testing:

Unfortunately, the level of completion in the finished prototype was not at a level to get proper magnetic validation data. Sensor firmware complications prevented us from implementing our intended method of measuring the produced magnetic field over space, and coil electrical malfunctions prevented us from producing any of the coil patterns that we designated as our basis vectors.

Fortunately, we made a contingency plan for this situation using a single-coil basis to test functional coils individually, and magneto chromic film to get a rough quantification of the magnetic field over space. As this film changes color proportionately to the local magnetic field, the color scale can be visually calibrated with a known dipole (a NdFeB button magnet) and used to roughly quantify the field intensity. The single-coil basis is much weaker than the multipole basis, which has an average of three coil's worth of power, but the maximum field intensity of around 1/3 T observed in the single-coil basis is consistent with a simulated system that produces a maximum dipole field of 0.8T.

Moreover, it was noticed during simulation that sub-optimal lens geometry would also limit the magnetic field intensity within the arena. In simulations within the arena, it was assumed that magnetic saturation of  $\sim 2\text{T}$  in the lens would be observed near the probe tips, allowing a maximum dipole moment of  $\frac{1}{2}$  saturation, or  $\sim 1\text{T}$ . Appendix E demonstrates that saturation in the lens (shown as maroon coloration in corresponding plots) didn't occur at the tips, but elsewhere in the lens for most configurations. More optimal geometry is possible to both make and fabricate by thickening the lens wherever unwanted saturation occurs, but we were fundamentally limited to using a consistent cross section in our lens for manufacturability.

It was also suspected that inconsistencies in composition/temper along our steel stock could introduce magnetic inconsistencies across our lens. The hot-rolling process is primarily focused on making structural steel as cheaply as possible. Magnetic variations across the material that don't affect structural performance aren't as important to control. Even though our research suggested that hot rolled steel was the best material for our application, experiments used physically smaller steel samples which would naturally lessen the impact of inconsistency on performance. As these effects subtly change the hysteresis loop of each lens component, they require spatial quantification of the magnetic field, and long-term testing. Neither demand is met by the prototype in its current state.

## **Electrical Testing:**

*Table F.2: Electrical Subsystem Verification Data.*

Electrical property	Specified value	Actual value*
Coil resistance Parallel Windings	25 $\Omega$	6 $\pm$ 0.375 $\Omega$
Coil resistance Series Windings**	100 $\Omega$	24 $\pm$ 1.5 $\Omega$
Driver Output Resistance	1.36 $\Omega$	Unverified
Drive Voltage (Max)	50 V	20 V
Drive Current (Max)	0.5 A	0.8 A
Coil MMF	> 1000 Amp turns	1080 Amp turns

\* Measured or derived from measurements using a Klein Tools MM200 multimeter.

\*\* Series winding configuration used in both specification and final prototype.

Electrical specifications of the assembled electromagnetic drive circuit were significantly different than the specified values. Due to time constraints, the specified 50V power delivery system was replaced with a commercial device used to drive brushed DC Motors. In this application, the motor coils are consistently biased with an external magnetic field, and more of the coil voltage is transferred to usable work. In this situation, low driver impedance is optimized for, as this maximizes the current, and thereby energy, that is delivered to each motor.

This is not the case for our prototype, coils only push against a small magnetic coercion, and most supplied energy is converted to heat. For slowly changing magnetic systems like ours, high driver impedance is crucial to minimizing joule heating. As a contingency plan for this, each coil winding was divided in two and connected in parallel, effectively quartering its impedance to better match the new drivers. As this contingency plan was an afterthought, the full consequences weren't considered, and issues with coil winding consistency compounded with the thin 28AWG wire. Slight mismatches in resistance between the two half-coils appeared to cause enough of a current imbalance to cause the lower resistance half to be destroyed, even at low drive power. This was

ultimately remedied by using fewer turns in a series configuration causing sub-optimal power transfer. Coil design with thicker wire was investigated, but an impedance match with 26AWG wire would have cost twice as much, with a rough trend of doubling the cost for every ~2AWG drop. For a prototype that functions as designed, sourcing a suitable high-voltage high-impedance driver is critical. Final demonstrations were conducted for short durations at increasing drive intensities to bypass any issues with heat generation, but long-term operation at power sufficient to produce specified drive (~2A) isn't possible.

Coil winding was controlled through counting the number of turns as this measure directly impacts magnetic performance. In the winding procedure, about 350 turns could be completed in perfect hexagonal packing before an unintentionally misplaced turn prevented all subsequent turns from continuing the packing, and coil winding took a faster & more chaotic approach (Easily visible on the outer coil surface in the finished prototype).

This shows a significant limitation in the coil winding apparatus, as a misplaced turn could be unwound & corrected, but since the drive, tensioning, and counting systems for the winding apparatus were only designed for one-way operation, a manual override procedure would need to take place. For this manual override, the jig would need to be partially disassembled, manually unwound, and all erroneous turns subtracted from the counter before hexagonally packed winding could resume. This procedure was attempted for early windings, but this practically doubled the wear on re-wound segments, which is a difficult to diagnose & highly variable source of failure. as well as the time to complete a winding, the packing scheme was shifted to be hexagonal wherever possible, and variations in coil resistance were accepted as unavoidable. This issue could be remedied by purchasing professionally assembled coils, the timeline of this project demanded

that damaged coils could be replaced quickly. With uncertainty in the actual performance of the assembled electrical system, less consistent coil resistance was deemed favorable to either over-purchasing or under-purchasing expensive pre-wound coils.

### **Mounting Verification:**

By positioning the clamp screws slightly below the midplane of the lens components, a slight torque is generated when the steel faces are mated. The central hub, formed HDPE and rubber spacers, holds each probe level when the system is uncompressed. When sufficiently compressed, the probes rise enough to produce an audible sound shift when the probe is tapped from above, evenly compressing the lens into close magnetic contact. This endpoint ensures that probes are level but doesn't necessarily demonstrate that the lens is in full magnetic contact.

Backing the clamping screws  $\frac{1}{2}$  turn below full compression allows the lens to expand by  $\sim 0.02''$  outwards at 24 threads per inch, which translates to a  $\sim 0.01''$  gap between mating faces. At this point, the probes slide in and out freely, which is consistent engineering fit tables for that tolerance. Under tension, the same engineering fit tables can be used to quantifiably verify that all components are within a  $0.005''$  tolerance of one another as all fits are too tight to move or adjust by hand.

Since steel's electrical and magnetic properties co-relate, magnetic contact and electrical contact co-occur. Since the steel-air gap difference is much more pronounced for electrical current than it is for magnetic flux, a junction that has good electrical contact has even better magnetic contact, and electrical resistivity between lens components can be used to verify magnetic contact. If any of the 15 pairs of probe components have a measurable electrical resistance between them, it indicates that two faces dividing the pair have poor contact. As no electrical resistance could be

measured on my multimeter between any pair of probes, it can be concluded that fewer than two faces have a resistance on the order of  $0.1\Omega$ . This test was validated by repeating it under partial compression, in which resistance was measured, and with masking tape obscuring the faces, making them perfect insulators. Testing the prototype's operation on iron filings in each situation also confirmed the importance of contact. Motion was significantly less under partial compression and virtually unnoticeable with the masking tape. Ultimately, we can conclude that lens fabrication and mounting system design was successful, even using a sub-optimal design.

Additional Notes:

Biocompatibility results verified using literature. Explanation of failure explored in body of report.

## Appendix G

### FYDP Resources

#### *Final Budget*

*Table G.1: Final budget sheet*

Item	Quantity	Cost (\$)	Reason for Purchase
XBOX One Wireless Controller	1	Preowned	Used to get user inputs on desired microrobot actuation.
Teensy 4.1	1	Preowned	Used to send user inputs to motor drivers.
Pololu Dual G2 High-Power Motor Driver 18v22 Shield for Arduino	3	Provided by Hamed Shahsavani	Used to provide current to the coils.
24 V Power Supply	1	Preowned	Used to provide power to coils.
DLP 405nm Resin	500 mL	Preowned	Used for thin films.
SU8 2100	50 ml	Provided by Mahla Poudineh	Used for thin films.
SU8 Developer	100 mL	Provided by Mahla Poudineh	Used for removing uncured SU8.
Microscope Slides	1 box	Provided by Hamed Shahsavani	Substrate for thin films and mask.
Brilliant Yellow	50 mL	Provided by Hamed Shahsavani	Sacrificial layer.
Acrylic laser printer clear paper	10 pages	Preowned	Mask printing.
Copper Tube 10'	1	12.49	Placed around iron bars to wrap coil.
1 ft x ½" x ¾" Hot-Rolled Iron Bar	8	14.87	Used for all iron cores.
28 AWG magnet wire	2 lb	87.42	Forms conductor in electromagnets.
Bismuth powder	~1g	preowned	Provides diamagnetic portion of oil bead actuators.
Ferrous Chloride	~ 1L	Home-made	Provides paramagnetic solution to suspend actuators.
Common Lab Reagents (Acetone, Ethanol, Isopropyl Alcohol)	As needed	Provided by Hamed Shahsavani	Cleaning components
Misc. building materials (HDPE, wood, screws, etc.)	As needed	Bought wholesale ~ 200	Physical construction of prototype.
Total Cost	N/A	314.78	N/A

*List of External Funds or Awards*

No external funds or awards were received.

*List of Lab Equipment*

Table G.2: List of lab equipment

Equipment Name	Owner	Reason
Spin coater	Dr. Hamed Shahsavan	Coating thin films
405nm Light Source	Dr. Hamed Shahsavan	Curing DLP
365nm UV Light Source	Dr. Hamed Shahsavan	Curing SU8
Microscope	Dr. Hamed Shahsavan	Optical verification of components
Glass Cutter	Dr. Hamed Shahsavan	Cutting microscope slides to size
Hot plate	Dr. Hamed Shahsavan	Soft baking thin films
UV Ozone Cleaner	Dr. Hamed Shahsavan	Cleaning glass substrate of organic components

*Team Member Contributions After Progress Update #3*

Table G.3: Team member contributions after progress update #3

Initials	Activity	Dates	Hours	Signatures
P	Modifying Pololu Arduino library	10/03	6	P.H.
P	Vector communication between computer & Teensy 4.1	16/03	2	P.H.
I	Fabricating & Wiring Faceplate	15/03	8	I.S.
I	Finalization of Wiring	15/03	3	I.S.
I	Electrical Testing and debugging	16/03	5	I.S.
I	Rewinding Burnt coils and insulating cores	16/03	5	I.S.
I	Writing controller C++ code for simple demonstrations	16/03	1	I.S.
K, A, I, P	Symposium Booth Presentations	17/03	5, 5, 5, 5	I.S., K.H., P.H., A.S.
K, A, I	FYDP Poster	01/03 – 17/03	10, 10, 1	I.S., K.H., A.S.
K, A, I, P	FYDP Presentation	01/03 – 17/03	25, 25, 3, 1	I.S., K.H., P.H., A.S.
K, A, I, P	FYDP Report	17/03 – 01/04	20, 20, 10, 20	I.S., K.H., P.H., A.S.